Molecular Cell

Article

PARP1 Links CHD2-Mediated Chromatin Expansion and H3.3 Deposition to DNA Repair by Non-homologous End-Joining

Graphical Abstract

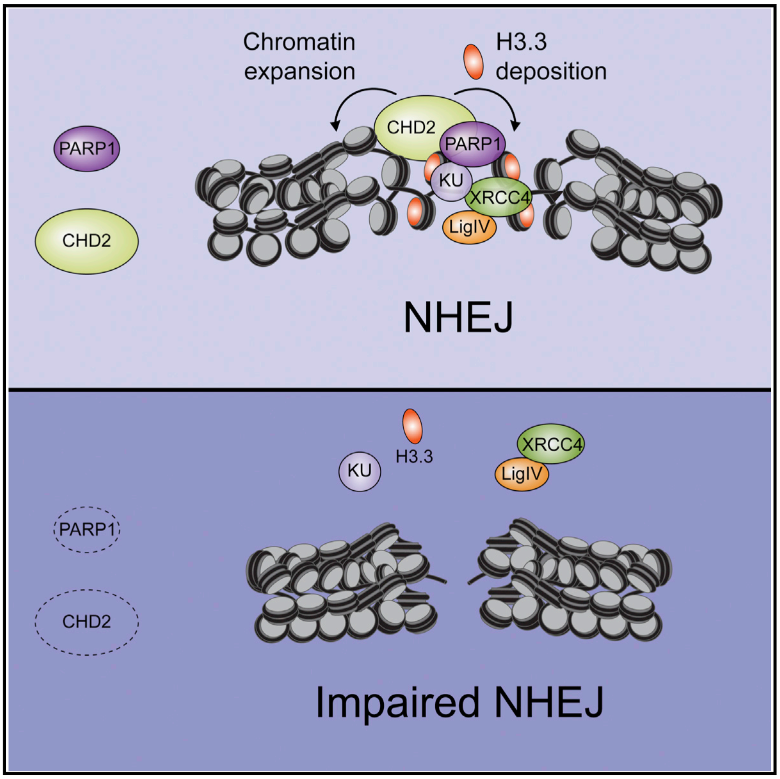

Authors

Martijn S. Luijsterburg, Inge de Krijger, Wouter W. Wiegant, ..., Jacqueline J.L. Jacobs, Girish M. Shah, Haico van Attikum

Correspondence

m.luijsterburg@lumc.nl (M.S.L.),
h.van.attikum@lumc.nl (H.v.A.)

In Brief

Luijsterburg et al. define a PARP1-dependent mechanism that regulates NHEJ through localized chromatin expansion and deposition of the histone variant H3.3 by the nucleosome remodeler CHD2 at DNA breaks. Their data also show that these CHD2-mediated events promote DNA repair by facilitating the assembly of NHEJ complexes in chromatin.

Highlights

- PARP1 recruits the chromatin remodeler CHD2 to DNA damage
- CHD2 promotes chromatin expansion and H3.3 deposition at DNA breaks
- CHD2 promotes the assembly of NHEJ repair complexes at DNA breaks
- PARP1 drives CHD2- and H3.3-dependent DNA repair by NHEJ

Luijsterburg et al., 2016, Molecular Cell *61*, 547–562
February 18, 2016 ©2016 The Authors
http://dx.doi.org/10.1016/j.molcel.2016.01.019

Molecular Cell
Article

PARP1 Links CHD2-Mediated Chromatin Expansion and H3.3 Deposition to DNA Repair by Non-homologous End-Joining

Martijn S. Luijsterburg,[1,*] Inge de Krijger,[2] Wouter W. Wiegant,[1] Rashmi G. Shah,[3] Godelieve Smeenk,[1]
Anton J.L. de Groot,[1] Alex Pines,[1] Alfred C.O. Vertegaal,[4] Jacqueline J.L. Jacobs,[2] Girish M. Shah,[3]
and Haico van Attikum[1,*]
[1]Department of Human Genetics, Leiden University Medical Center, Einthovenweg 20, 2333 ZC Leiden, the Netherlands
[2]Division of Molecular Oncology, The Netherlands Cancer Institute, Plesmanlaan 121, 1066 CX Amsterdam, the Netherlands
[3]Laboratory for Skin Cancer Research, CHU-Q: University Hospital Research Centre of Quebec (CHUL site) and Laval University, Quebec City, QC G1V 4G2, Canada
[4]Department of Molecular Cell Biology, Leiden University Medical Center, Einthovenweg 20, 2333 ZC Leiden, the Netherlands
*Correspondence: m.luijsterburg@lumc.nl (M.S.L.), h.van.attikum@lumc.nl (H.v.A.)

http://dx.doi.org/10.1016/j.molcel.2016.01.019

SUMMARY

The response to DNA double-strand breaks (DSBs) requires alterations in chromatin structure to promote the assembly of repair complexes on broken chromosomes. Non-homologous end-joining (NHEJ) is the dominant DSB repair pathway in human cells, but our understanding of how it operates in chromatin is limited. Here, we define a mechanism that plays a crucial role in regulating NHEJ in chromatin. This mechanism is initiated by DNA damage-associated poly(ADP-ribose) polymerase 1 (PARP1), which recruits the chromatin remodeler CHD2 through a poly(ADP-ribose)-binding domain. CHD2 in turn triggers rapid chromatin expansion and the deposition of histone variant H3.3 at sites of DNA damage. Importantly, we find that PARP1, CHD2, and H3.3 regulate the assembly of NHEJ complexes at broken chromosomes to promote efficient DNA repair. Together, these findings reveal a PARP1-dependent process that couples ATP-dependent chromatin remodeling with histone variant deposition at DSBs to facilitate NHEJ and safeguard genomic stability.

INTRODUCTION

DNA double-strand breaks (DSBs) are a considerable threat to the integrity of the human genome and, if not properly dealt with, can cause genomic instability and cancer. The response to DSBs entails a coordinated series of events known as the DNA damage response (DDR), which integrates the regulation of cell cycle progression with DSB repair mechanisms through DNA damage signaling pathways (Polo and Jackson, 2011).

In eukaryotes, DSBs are primarily repaired by two pathways: homologous recombination (HR) and non-homologous end-joining (NHEJ). HR operates in the S and G2 stages of the cell cycle and requires extensive resection of DSBs to generate stretches of single-stranded DNA, which are acted upon by the single-stranded DNA-binding protein RPA and the recombinase RAD51. These and other factors subsequently facilitate the error-free repair of DSBs by using the sister chromatid as a template (Symington and Gautier, 2011). In contrast, NHEJ, which is the dominant DSB repair pathway in mammalian cells, requires minimal DNA-end processing. Initiation of NHEJ involves the binding of the KU70-KU80 complex to broken DNA ends followed by the assembly of the DNA-dependent protein kinase (DNA-PK) and the XRCC4-LigIV complex (Lieber, 2010).

DSB repair takes place on genomic DNA that is packaged together with histone proteins into an often-inaccessible structure called chromatin. Regulating the accessibility of damaged DNA requires a high degree of coordination between DSB repair machineries and chromatin-modifying enzymes (Luijsterburg and van Attikum, 2011; Smeenk and van Attikum, 2013).

Initial studies using photo-activatable GFP fused to the core histone H2B revealed that DNA damage triggers the localized expansion of chromatin in an ATP-dependent fashion (Kruhlak et al., 2006). Subsequent studies uncovered that this localized chromatin expansion requires the activity of poly(ADP-ribose) polymerase (PARP) enzymes and promotes DNA damage signaling by the RNF168 ubiquitin ligase (Smeenk et al., 2013). The initial rapid expansion of chromatin is followed by the localized compaction of chromatin (Burgess et al., 2014; Khurana et al., 2014), suggesting that specific chromatin configurations regulate different aspects of the DDR. In particular, localized chromatin compaction, which is regulated by the PRDM2 histone methyltransferase, regulates DNA-end resection and promotes DSB repair by HR (Khurana et al., 2014). In addition to chromatin compaction, a number of ATP-dependent chromatin remodelers (e.g., SMARCAD1, INO80, p400, and CHD4) that are usually associated with chromatin decondensation have also been linked to regulating end resection or other steps during HR (Smeenk and van Attikum, 2013). These findings suggest that HR is tightly regulated by dynamic changes in chromatin structure.

Despite these considerable insights into dynamic changes in chromatin structure during DNA damage signaling and HR, we

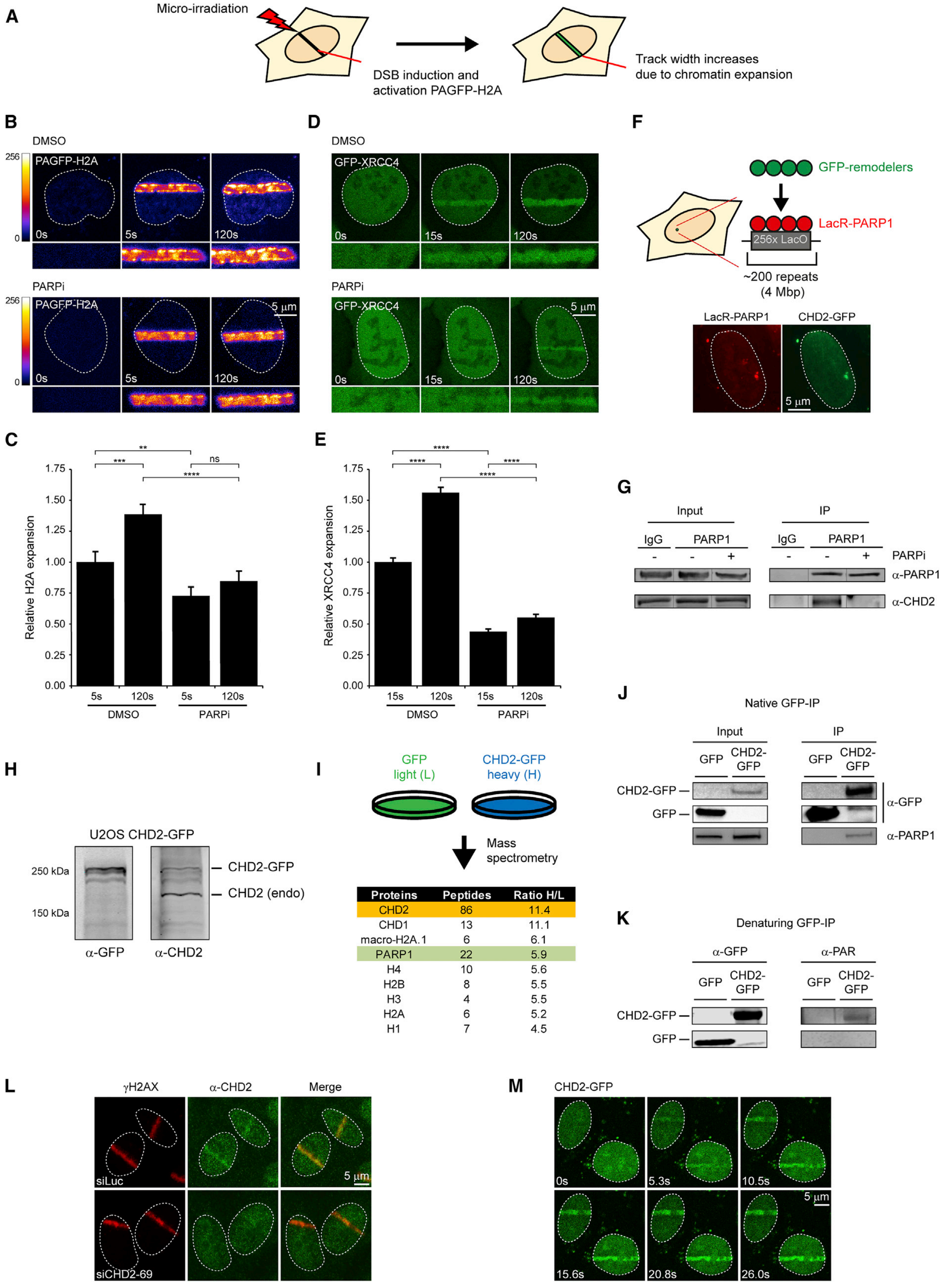

Proteins	Peptides	Ratio H/L
CHD2	86	11.4
CHD1	13	11.1
macro-H2A.1	6	6.1
PARP1	22	5.9
H4	10	5.6
H2B	8	5.5
H3	4	5.5
H2A	6	5.2
H1	7	4.5

(legend on next page)

know very little about alterations in chromatin structure that may play a role in NHEJ. To fill this gap, we sought to characterize chromatin changes that play a role in NHEJ in human cells and identify a previously uncharacterized pathway involved in this process.

RESULTS

PARP1 Promotes Chromatin Expansion and Spreading of NHEJ Factor XRCC4

We sought to characterize changes in chromatin structure in response to DNA damage that may play a role in NHEJ. To this end, we revisited a method to locally inflict DNA damage and simultaneously activate histone H2A fused to a photo-activatable version of GFP (PA-GFP) using multiphoton micro-irradiation (Figure 1A) (Kruhlak et al., 2006; Smeenk et al., 2013). Local irradiation triggered the rapid expansion of PAGFP-H2A tracks in control cells, but not in cells treated with the PARP inhibitor (Figures 1B and 1C), suggesting that DNA damage-induced chromatin changes depend on the activity of PARP enzymes. To monitor possible chromatin changes involved in NHEJ, we generated U2OS cells stably expressing a GFP-tagged version of the core NHEJ protein XRCC4. Local irradiation triggered the accumulation of GFP-XRCC4 in laser tracks, which displayed considerable expansion over time (Figures 1D and 1E). Strikingly, treatment of cells with PARP inhibitor or knockdown of PARP1 significantly reduced the expansion of GFP-XRCC4 tracks, suggesting that PARP1-dependent changes in chromatin structure may play a role in NHEJ (Figures 1D and 1E; Figures S1A and S1B).

The Chromatin Remodeler CHD2 Is an Interactor of PARP1

We then set out to identify factors that regulate these chromatin changes by analyzing PARP1-associated chromatin-modifying proteins using a previously described chromatin-tethering approach (Luijsterburg et al., 2012a). To this end, we fused PARP1 to the lactose repressor protein (LacR) and expressed the fusion protein in U2OS cells harboring stably integrated LacO repeats. These cells were subsequently transfected with a representative collection of GFP-tagged SWI2/SNF2 ATPases from the four major chromatin remodeling families (SWI/SNF, ISWI, INO80, and CHD). This approach identified the chromodomain helicase DNA-binding protein 2 (CHD2) as a possible interactor of PARP1 (Figure 1F; Figure S1C). Co-immunoprecipitation (coIP) confirmed the interaction between endogenous PARP1 and CHD2, which was completely abolished by treatment with PARP inhibitor (Figure 1G). This suggests that the association between CHD2 and PARP1 is not mediated by protein-protein interactions but may involve the association of CHD2 with poly(ADP-ribose) (PAR) chains on PARP1 (Figure 1G).

To further study the interaction between CHD2 and PARP1, we stably expressed GFP-tagged CHD2 in U2OS cells at levels roughly similar to endogenous CHD2 (Figure 1H). Immunoprecipitation of CHD2-GFP followed by mass spectrometry (MS) after SILAC revealed 139 proteins that were at least 2-fold enriched compared with control cells (Table S1). This analysis not only revealed interactions with all core histones and the related chromatin remodeler CHD1, but it also confirmed PARP1 as a robust CHD2-interacting protein (Figure 1I). CoIP analysis of CHD2-GFP revealed endogenous PARP1 in the IP fraction, further establishing this interaction (Figure 1J). To test if CHD2 is a substrate of PARP1, we immunoprecipitated GFP or CHD2-GFP from cells under denaturing conditions and analyzed their PARylation status by western blotting. This revealed that CHD2 is indeed a substrate of poly(ADP-ribosyl)ation (Figure 1K). We conclude that CHD2 is an interactor of PARP1 and decided to study its role in DSB repair.

CHD2 Accumulates at Sites of DNA Damage

To determine if CHD2 acts locally at sites of DNA damage, we tested its recruitment to laser-inflicted DNA DSBs. Endogenous CHD2 was rapidly recruited to DNA damage tracks marked by γH2AX following UV-A micro-irradiation (Figure 1L) or multiphoton laser irradiation (Figure 2C). Control experiments showed that siRNA-mediated knockdown of CHD2 abolished CHD2 signals in laser tracks, demonstrating the specificity of the CHD2 antibody (Figure 1L). Moreover, GFP-tagged CHD2 also rapidly localized to sites of laser-induced DNA damage in both G1 and S/G2 cells (Figure 1M; Figures S1D and S1E). These findings show that CHD2 is recruited to sites of DNA damage.

PARP1 Recruits CHD2 to Sites of DNA Damage

To assess a potential role of PARP1's catalytic activity in CHD2 recruitment to sites of DNA damage, we measured the association kinetics of CHD2 using live-cell imaging. A time-course analysis revealed that the rapid ($t_{1/2}$ = 5 s) accumulation of CHD2 reached a maximum around ~1 min after which the steady-state

Figure 1. Chromatin Changes in Response to DNA Damage Depend on PARP1

(A) Outline of the chromatin expansion approach.

(B) PAGFP-H2A expansion in U2OS cells treated with DMSO or 10 μM PARPi.

(C) Quantification of (B).

(D) GFP-XRCC4 expansion in U2OS cells treated with DMSO or 10 μM PARPi.

(E) Quantification of (D). 40–65 cells were analyzed from three independent experiments.

(F) Outline of the chromatin-tethering approach in U2OS 2-6-3 cells, which identified CHD2 as a PARP1 interactor.

(G) CoIP of endogenous PARP1 and CHD2 in HEK293 cells.

(H) Western blot on U2OS CHD2-GFP cells.

(I) SILAC of HEK293 cells expressing GFP (L) or CHD2-GFP (H).

(J) CoIP of CHD2-GFP and endogenous PARP1 in HEK293 cells.

(K) PARylation of CHD2-GFP in HEK293 cells.

(L) Recruitment of endogenous CHD2 to UV-A tracks in U2OS cells. CHD2 knockdown confirms antibody specificity.

(M) Recruitment of CHD2-GFP to multi-photon tracks in U2OS cells.

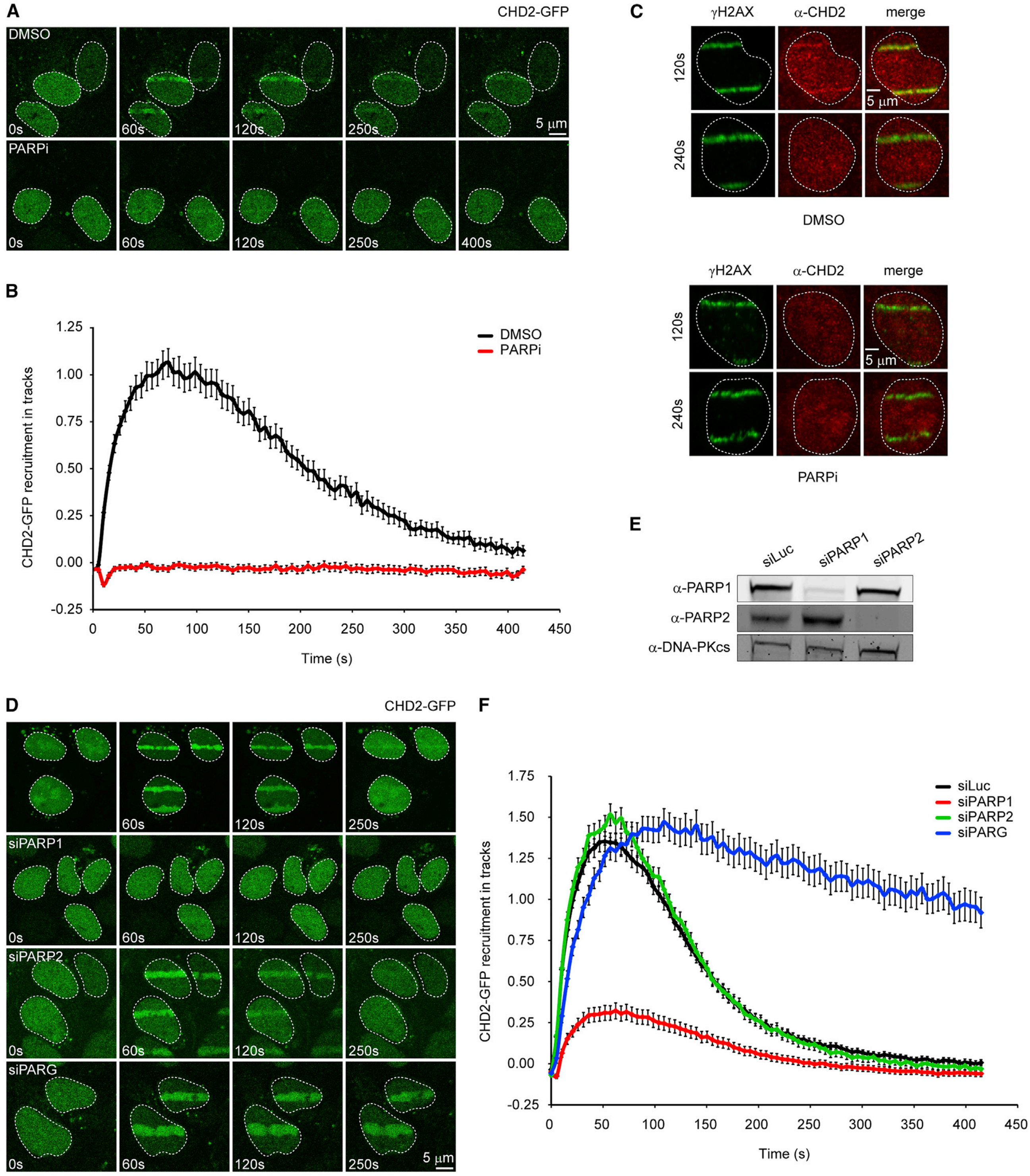

Figure 2. CHD2 Recruitment to DNA Damage Requires PARP1

(A) Recruitment of CHD2-GFP to multi-photon tracks in U2OS cells treated with DMSO or 1 μM PARPi.

(B) Quantification of (A).

(C) Recruitment of endogenous CHD2 in U2OS cells treated with DMSO or 10 μM PARPi.

(D) Recruitment of CHD2-GFP in cells transfected with the indicated siRNAs.

(E) Western blot showing PARP1/2 knockdown efficiency in cells from (D).

(F) Quantification of (D). 30–170 cells were analyzed from three independent experiments.

bound levels gradually decreased within ~5 min (Figures 2A and B). Treatment of cells with PARP inhibitor, which prevented PAR chain formation in laser tracks (Figure S1F), completely abolished the recruitment of CHD2-GFP (Figures 2A and 2B), as well as that of endogenous CHD2 into γH2AX-positive laser tracks (Figure 2C). This effect was phenocopied by siRNA-mediated depletion of PARP1, but not PARP2 (Figures 2D–2F), suggesting that CHD2 recruitment is strictly dependent on PARP1. Although PARP1 is responsible for ~85% of the synthesized PAR chains in response to DNA damage, such chains are rapidly hydrolyzed by the activity of poly(ADP-ribose) glycohydrolase 1 (PARG), which explains the rapid turnover of PAR chains at sites of DNA damage (Pines et al., 2013). To prevent this rapid turnover, we increased the steady-state levels of chromatin-associated PAR chains by depletion of PARG (Luijsterburg et al., 2012b). Live-cell imaging showed that PARG knockdown dramatically increased the retention time of CHD2 on damaged chromatin (Figures 2D and 2F). To extend these findings, we overexpressed mCherry-tagged PARG^{WT} or catalytically dead $\text{PARG}^{\text{E756D}}$ (Ismail et al., 2012), which completely suppressed CHD2-GFP recruitment (Figures S1G and S1H). Of note, catalytically dead PARG accumulated more strongly likely due to its inability to hydrolyze PAR chains, suggesting that this mutant protein may suppress CHD2 recruitment by direct competition for PAR binding. In conclusion, CHD2 recruitment to DSB-containing chromatin requires the PARP1-mediated synthesis of PAR chains.

A Conserved Region in CHD2 Mediates DNA Damage Accumulation and PAR Binding

To gain more insight into how CHD2 is recruited in a PAR-dependent manner, we generated a series of deletion mutants spanning the whole CHD2 protein (Figure 3A). Immunoblotting confirmed that the GFP-tagged deletion mutants were expressed at the correct molecular weight (Figure 3B). We then co-expressed these mutant proteins with NBS1-mCherry in cells depleted for endogenous CHD2 and subsequently assessed their ability to accumulate at DSBs. Regions of CHD2 spanning its chromodomains ($\text{CHD2}^{1\text{–}461}$), ATPase/helicase domains ($\text{CHD2}^{462\text{–}951}$) or putative SANT-SLIDE motif ($\text{CHD2}^{952\text{–}1391}$; Figure S2A) failed to accumulate in cells that did accumulate NBS1-mCherry (Figures 3C and 3D). Conversely, $\text{CHD2}^{1392\text{–}1828}$ robustly accumulated in laser tracks (Figures 3C and 3D). An in silico analysis of the minimal recruitment region identified a putative PAR-binding motif that almost matches the consensus (Figure S2B) (Gagné et al., 2008). Surprisingly, however, a region encompassing this putative PAR-binding region ($\text{CHD2}^{1392\text{–}1610}$) failed to accumulate (Figures 3C and 3D) even when fused to an NLS (Figure S2C), whereas the last C-terminal ~200 amino acids ($\text{CHD2}^{1611\text{–}1828}$) were sufficient to mediate PAR-dependent accrual at DSBs (Figures 3C and 3D). Indeed, full-length CHD2 lacking this region ($\text{CHD2}^{1\text{–}1610}$) failed to accumulate at DSBs (Figures 3C and 3D), suggesting that the region spanning residues 1611–1828 regulates the PAR-dependent recruitment of CHD2. To further corroborate these findings, we carried out in vitro PAR-binding studies by incubating immunoprecipitated GFP-tagged wild-type and mutant CHD2 protein with ^{32}P-radiolabeled PAR chains using southwestern blotting. This revealed that both CHD2^{WT} and $\text{CHD2}^{1611\text{–}1828}$ indeed bind PAR chains with equal efficiency (Figures 3E and 3F). Although it did not support recruitment to laser tracks (Figures 3C and 3D), we could also detect PAR binding of $\text{CHD2}^{1392\text{–}1610}$, albeit almost 3-fold weaker compared to the minimal recruitment region ($\text{CHD2}^{1611\text{–}1828}$) (Figures 3E and 3F). Southwestern analysis with recombinant proteins confirmed the ~3-fold stronger association of $\text{CHD2}^{1611\text{–}1828}$ with PAR chains in vitro compared to $\text{CHD2}^{1392\text{–}1610}$ (Figure S2D). Notably, the $\text{CHD2}^{1392\text{–}1610}$ fragment failed to support PAR binding in the context of the larger CHD2 protein because we did not detect appreciable PAR binding for the $\text{CHD2}^{1\text{–}1610}$ mutant containing this region (Figures 3E and 3F). Of note, coIPs showed that $\text{CHD2}^{1611\text{–}1828}$ interacted only weakly with PARP1, whereas CHD2^{WT} and $\text{CHD2}^{1\text{–}1610}$ robustly pulled down PARP1 (Figure 3E), suggesting that the PAR-binding region is distinct from the PARP1-interacting region. Indeed, we found that fragment $\text{CHD2}^{1392\text{–}1610}$, which failed to support recruitment to sites of DNA damage, was sufficient to bind PARP1 (Figure 3E). In conclusion, we have mapped the PAR-binding region in CHD2 and show that this region is sufficient and required for CHD2 recruitment to DSBs.

CHD2 Protects Human Cells against IR

To test whether the recruitment of CHD2 bears any functional significance for DSB repair, we addressed whether this chromatin remodeler protects human cells against the deleterious consequences of ionizing radiation (IR)-induced DSBs. Depletion of CHD2 from SV40-immortalized VH10 human fibroblasts using three independent siRNAs reduced the clonogenic survival of these cells after IR to the same extent as knockdown of DSB repair factor XRCC4 (Figure 4A; Figure S3A). To corroborate these findings, we stably expressed three different shRNAs targeting CHD2 and one shRNA against the key DDR kinase ATM in hTERT-immortalized VH10 human fibroblasts. This approach confirmed that loss of CHD2 renders human cells highly sensitive to IR (Figure S3B) and raises the question how CHD2 is involved in DSB repair.

CHD2 Promotes DSB Repair by NHEJ

Chromosomal DSBs are repaired by HR or NHEJ. To test if CHD2 may be involved in these DSB repair pathways, we utilized GFP-based assays that rely on the repair of DSBs in the *GFP* gene generated by the I-SceI endonuclease. Flow cytometric analysis of DR-GFP reporter cells for HR (Figure S3C) showed a dramatic increase in GFP-positive cells following I-SceI expression, which was severely suppressed by siRNA-mediated depletion of the core HR factor BRCA2 (Figure S3D). However, three independent siRNAs against CHD2 did not substantially impair repair by HR and neither did depletion of the core NHEJ factor XRCC4 (Figures S3D and S3E). In addition, RAD51 foci formation after IR in S-phase cells was also not affected by depletion of CHD2, confirming that CHD2 does not promote HR (Figures S3F and S3G).

Conversely, analysis of EJ5-GFP reporter cells for NHEJ (Figure 4B) revealed a reproducible decrease in NHEJ efficiency upon depletion of CHD2 by six independent siRNAs, which was comparable to the defect observed after depletion of XRCC4 (Figure 4C; Figure S4A). As expected, depletion of the HR factor BRCA2 did not affect NHEJ (Figure 4C). The

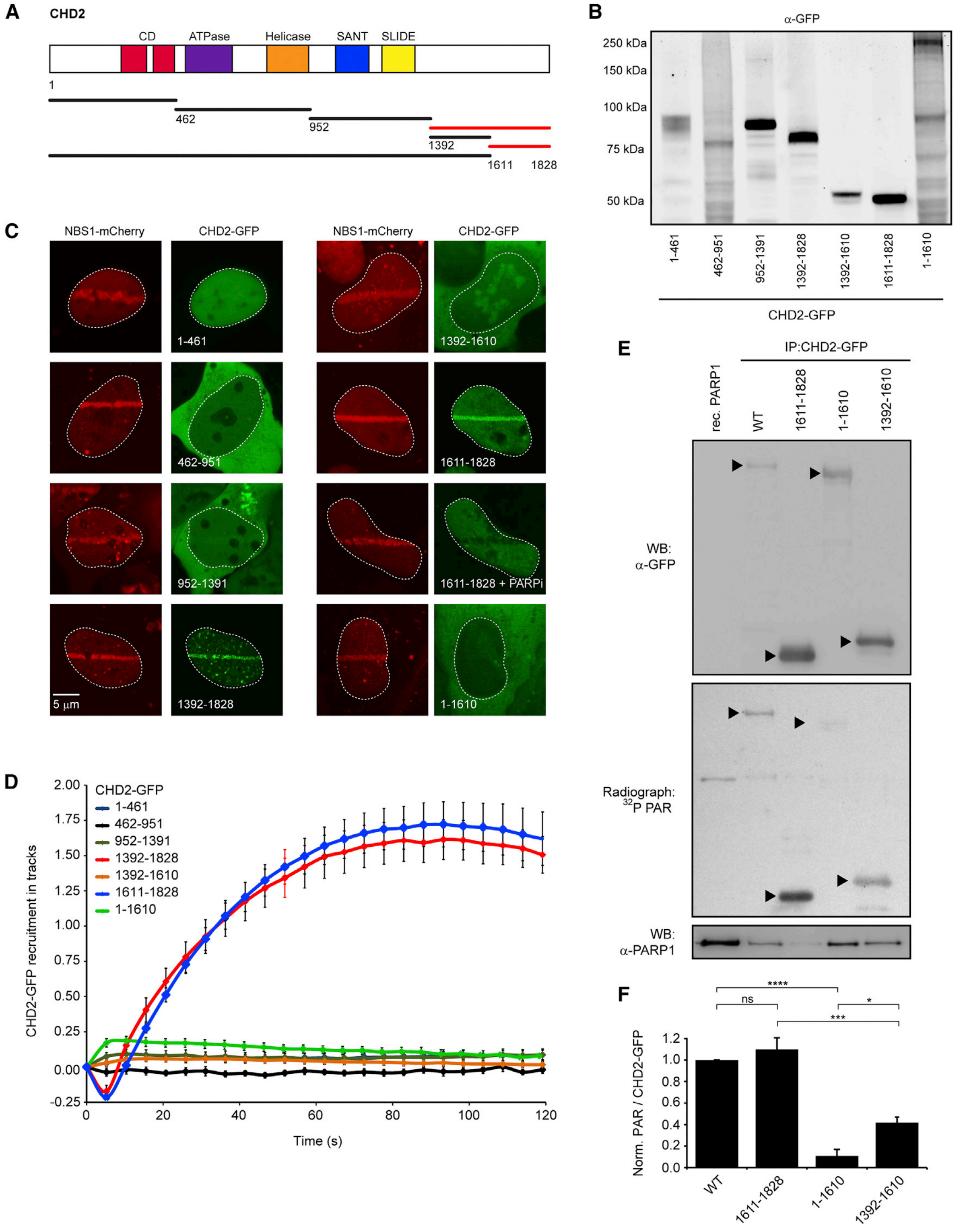

Figure 3. The C Terminus of CHD2 Is Required for DNA Damage Recruitment and PAR Binding

(A) Schematic representation of CHD2 and its deletion mutants.

(B) Western blot showing expression of the mutants from A in U2OS cells.

(C) Recruitment of CHD2-GFP deletion mutants in cells depleted for endogenous CHD2 by siCHD2-69 or siCHD2-17 in case of CHD2$^{952–1391}$-GFP. CHD2$^{1–1611}$-GFP was rendered siCHD2-69-resistant. NBS1-mCherry was a DNA damage marker.

(D) Quantification of (C). 10–30 cells were analyzed from two independent experiments.

(E) IP of the indicated CHD2-GFP fragments from HEK293 cells followed by southwestern blotting to monitor association with radiolabeled PAR. Recombinant PARP1 was a control. CoIP with endogenous PARP1 is shown in the bottom panel.

(F) Quantification of (E) and two additional independent experiments. PAR binding levels of CHD2^{WT}-GFP were set to 1.

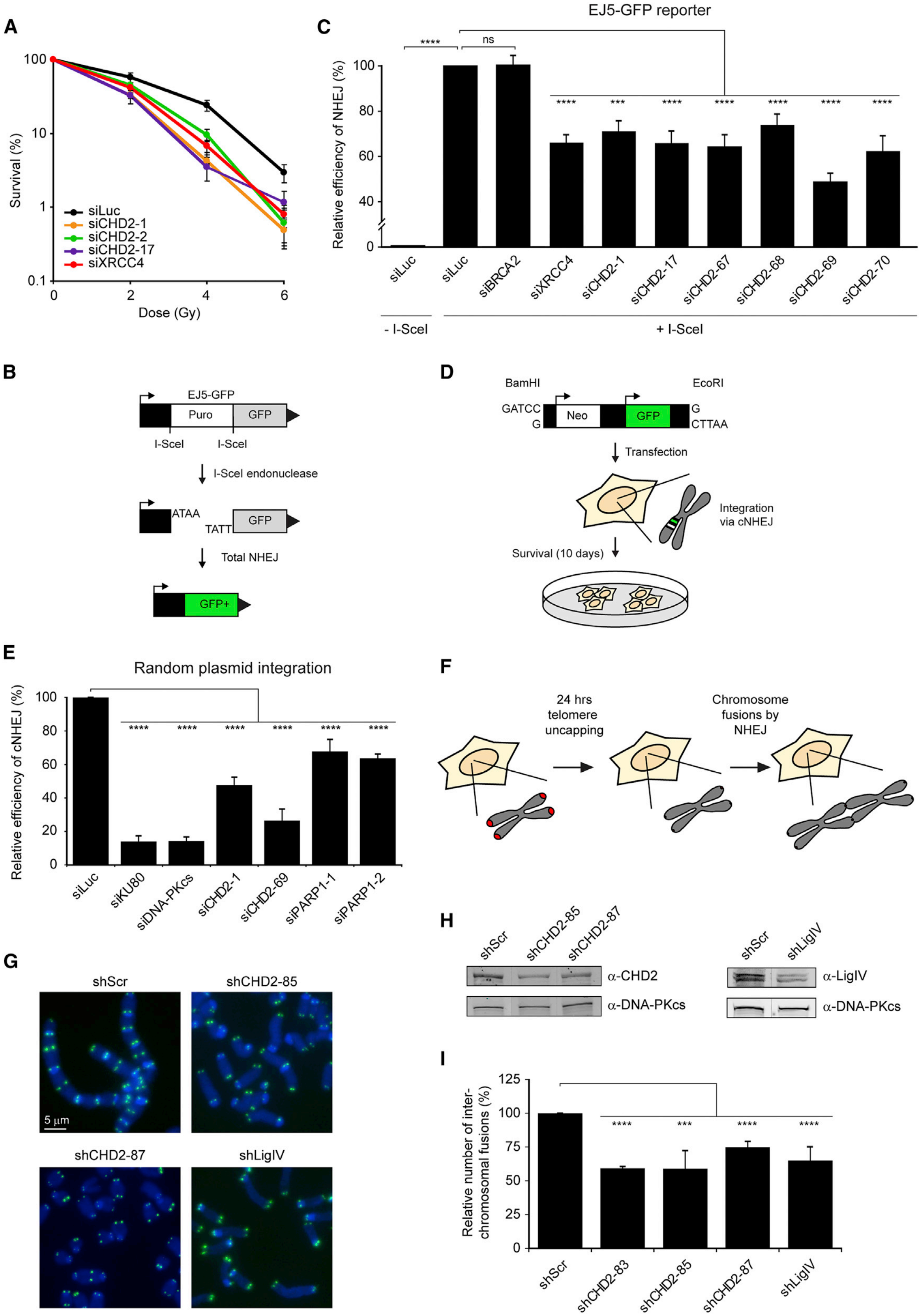

(legend on next page)

EJ5-GFP reporter provides a readout for total NHEJ activity, but it is not specific for canonical NHEJ (cNHEJ) or alternative NHEJ (aNHEJ), which comprise the two major pathways of NHEJ (Bennardo et al., 2008). To address if PARP1 and CHD2 play a role in cNHEJ, we used random plasmid integration into genomic DNA as a measure for cNHEJ (Figure 4D) (Galanty et al., 2009). Knockdown of the core NHEJ factors KU80 or DNA-PKcs nearly abrogated plasmid integration, confirming that this process largely depends on cNHEJ (Figure 4E; Figure S4B). Significantly reduced cNHEJ activity was also observed following depletion of either CHD2 or PARP1 with two independent siRNAs per gene (Figure 4E; Figure S4B), suggesting that both of these factors contribute to DSB repair by cNHEJ. Importantly, knockdown of CHD2 did not affect the steady-state levels of NHEJ proteins or PARP1 arguing against indirect effects due to transcriptional misregulation (Figure S4C).

As an alternative means to study NHEJ, we exploited the notion that loss of the shelterin complex at telomeres causes NHEJ-dependent chromosome-end fusions (Smogorzewska et al., 2002). To study the role of CHD2 in this process, we used mouse embryonic fibroblasts containing a temperature-sensitive allele of the shelterin protein TRF2 (TRF2^{ts}) (Boersma et al., 2015). At the non-permissive temperature of 39°C, TRF2^{ts}-mediated telomere protection is lost, subsequently triggering the NHEJ-dependent fusion of uncapped chromosome ends (Figure 4F). Strikingly, knockdown of CHD2 by three individual shRNAs significantly lowered the number of fused chromosomes in comparison to a control shRNA in TRF2^{ts} cells grown at non-permissive temperatures (Figures 4G–4I; Figure S4D). A comparable decrease in chromosome-end fusions was observed in cells depleted for the core NHEJ factor LigIV (Figures 4G–4I). In line with previous findings (Sfeir and de Lange, 2012), we found that knockdown of PARP1, in contrast to CHD2 knockdown, did not reduce the formation of NHEJ-mediated chromosome fusions (Figures S4E and S4F), suggesting that at uncapped telomeres, CHD2 may act through a PARP1-independent mechanism. These findings suggest that CHD2 contributes to cNHEJ activity in mouse cells and, as such, promotes chromosome-end fusions at uncapped telomeres. Thus, although dispensable for repair by HR, our findings implicate CHD2 in DSB repair by NHEJ. We next set out to determine how CHD2 affects this DSB repair pathway.

CHD2 Promotes the Recruitment of Core NHEJ Factors

The repair of chromosomal DSBs by NHEJ depends on the binding of the KU70-KU80 dimer to broken DNA ends followed by the recruitment of the DNA-PKcs kinase (Mari et al., 2006). The XRCC4-LigIV complex is subsequently recruited to DSBs to seal the break. To monitor interactions between CHD2 and NHEJ proteins, we performed reciprocal coIP experiments, which revealed an interaction between endogenous CHD2 and endogenous KU70 (Figure 5A) or GFP-tagged KU70 (Figure S4G). Notably, this interaction was not affected by PARP inhibition or IR-induced DNA damage (Figure S4G). To subsequently test if CHD2 promotes the recruitment of NHEJ factors, we monitored their accumulation at DSBs by live-cell imaging using cells stably expressing GFP-tagged KU70 (Mari et al., 2006) or GFP-tagged XRCC4. Multiphoton micro-irradiation triggered rapid GFP-KU70 recruitment to DSBs within several seconds ($t_{1/2}$ = 5 s; Figure 5B), whereas GFP-XRCC4 accrual was significantly slower ($t_{1/2}$ = 25 s; Figure 5C). Importantly, the detection of KU70 in laser tracks required much high laser power than that of XRCC4, suggesting that these factors do not accumulate at the same stoichiometric amounts (Figure S4H). Importantly, the depletion of CHD2 by two independent siRNAs significantly suppressed both GFP-KU70 (Figure 5B) and GFP-XRCC4 (Figure 5C; Figure S4I) recruitment to laser-generated DSBs, whereas the recruitment of GFP-XRCC1 to single-stranded breaks was unaffected (Figures S4J–S4L). As expected, GFP-XRCC4 recruitment in these cells was fully dependent on functional KU80 (Figure 5C). Moreover, the recruitment of endogenous XRCC4 was also suppressed in CHD2-depleted cells after micro-irradiation (Figures S5A–S5D) and at nuclease-induced DSBs (Figure 5D). The levels of localized γH2AX in control or CHD2-depleted cells were similar, showing that CHD2 depletion did not affect DNA damage induction (Figure 5D; Figure S5C). At the single-cell level, we confirmed that cells with decreased GFP-XRCC4 accrual following depletion of CHD2 failed to accumulate endogenous CHD2 in laser tracks, whereas CHD2 did clearly accumulate in control cells (Figure S5E). Notably, overexpression of ATPase-dead CHD2 (K515R; Figure S5F), but not wild-type CHD2, also reduced the recruitment of XRCC4 (Figure 5E). Together, these findings suggest that the chromatin remodeling activity of CHD2 promotes the efficient assembly of NHEJ complexes at DSBs.

Given that CHD2 recruitment is PARP1 dependent, we next asked whether the CHD2-mediated recruitment of XRCC4 to damaged chromatin relies on PARP1. Micro-irradiation experiments showed that treatment of cells with PARP inhibitor (Figure 5F) or siRNAs against PARP1 (Figure 5G; Figure S5G) significantly suppressed GFP-XRCC4 accumulation at

Figure 4. CHD2 Promotes DSB Repair by NHEJ

(A) Clonogenic survival after IR exposure of VH10-SV40 cells transfected with the indicated siRNAs.

(B) Schematic representation of the EJ5-GFP reporter for NHEJ.

(C) Quantification of EJ5-GFP-positive HEK293 cells corrected for I-SceI transfection efficiency by co-transfection with mCherry. The average of four independent experiments is shown.

(D) Schematic representation of the plasmid integration assay.

(E) Quantification of the plasmid integration efficiency in U2OS cells from three independent experiments.

(F) TRF2^{ts} MEFs were shifted to the non-permissive temperature to induce telomere uncapping and NHEJ-dependent chromosome fusions.

(G) Representative images of metaphases from TRF2^{ts} MEFs transduced with the indicated shRNAs after 24 hr of telomere uncapping. Telomere-FISH shows the position of the telomeres (green), and chromosomes are stained by DAPI (blue).

(H) Western blot showing CHD2 and LigIV knockdown efficiency in TRF2^{ts} MEFs.

(I) Quantification of interchromosomal fusions observed in cells transduced with the indicated shRNAs. Scrambled control shRNA (shScr) was normalized to 100%. 4500–8000 chromosomes were analyzed from three to eight independent experiments.

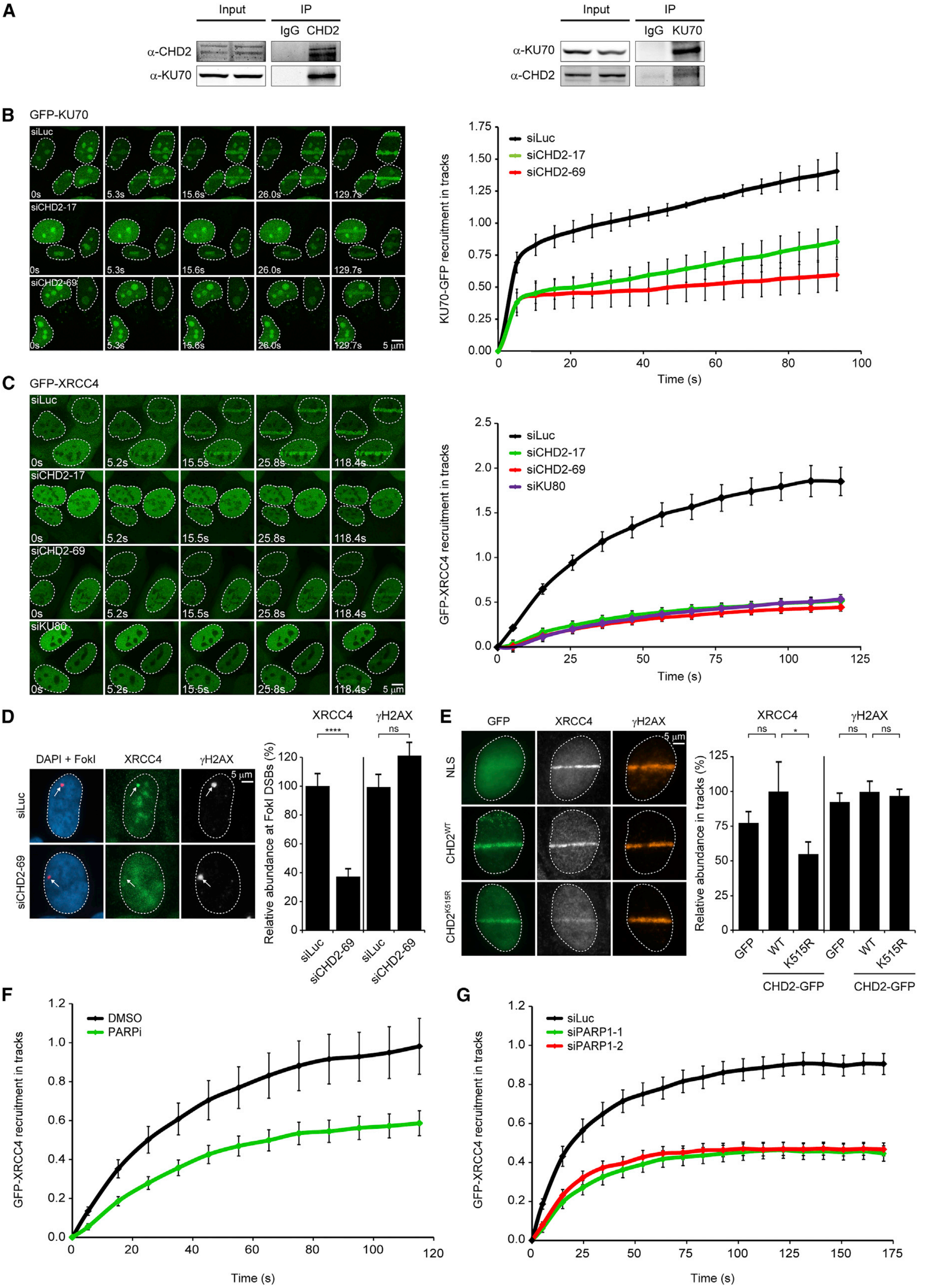

(legend on next page)

laser-generated DSBs. We conclude that PARP1-mediated recruitment of CHD2 is required for the efficient assembly of NHEJ factors.

CHD2 Promotes Chromatin Changes in Response to DNA Damage

The fact that the PARP1-mediated recruitment of CHD2 promotes the assembly of NHEJ complexes raises the question of whether this phenomenon requires CHD2-mediated chromatin remodeling. We first assessed whether CHD2 is capable of mediating large-scale chromatin unfolding by utilizing an in vivo chromatin-remodeling assay (Figure 6A). Human U2OS cells harboring a 4-Mbp heterochromatic region containing lactose operator (LacO) repeats were transfected with a plasmid encoding a LacR-tagged single-domain GFP antibody. The resulting fusion protein (αGFP-LacR) efficiently tethered co-expressed GFP-tagged proteins to the LacO array (Figure 6A). Tethering of wild-type CHD2-GFP elicited a 2-fold expansion of chromatin at the LacO array compared to tethering GFP only (Figure 6B). However, ATPase-dead CHD2 (K515R; Figure S5F) failed to unfold chromatin, even though it was recruited as efficiently as wild-type CHD2 (Figure S6A), whereas a mutant lacking its PAR-binding motif (Δ1611–1828; Figure 3) was proficient in mediating chromatin unfolding (Figures 6A and 6B). These findings confirm that CHD2 is an ATP-dependent chromatin remodeler and that its PAR-binding motif (1611–1828) is dispensable for its chromatin-remodeling function.

We next investigated if CHD2 would be required for DNA damage-induced chromatin changes. To this end, we co-expressed NBS1-mCherry together with histone H2A fused to PAGFP-H2A (Figures 1B and 6C). Laser micro-irradiation triggered robust recruitment of NBS1 and localized activation of PAGFP-H2A in tracks, which rapidly expanded within the first minutes after irradiation indicative of DNA damage-induced chromatin changes (Figures 6D and 6F). Expansion of PAGFP-H2A occurred in both G1 and S/G2 cells (Figure S6B) and was not observed in chemically fixed cells (Figures S6C and S6E), showing that it represents a cell cycle-independent biological phenomenon that is induced by DNA damage. Importantly, when we used laser conditions that efficiently activated PAGFP-H2A and led to recruitment of single-strand break repair factor GFP-XRCC1 but failed to recruit DSB repair factor XRCC4, we did not detect any expansion of H2A tracks (Figures S6D–S6I). These findings suggest that laser-induced chromatin changes are linked to the generation of DSBs. Having established conditions to detect DSB-induced chromatin changes, we next examined whether CHD2 is required for these events. Knockdown of CHD2 using two independent siRNAs substantially reduced expansion of PAGFP-H2A (Figures 6E and 6F; Figures S6E and S6J), whereas CHD4 or SNF2H depletion did not affect this process (Figures S6K and S6L). Similarly, knockdown of CHD2 also impaired unfolding of LacO arrays following DSB induction by the FokI nuclease (Figure 6G). Consistent with the PARP1-mediated recruitment of CHD2, we found that the depletion of PARP1 efficiently antagonized chromatin expansion (Figure 6F; Figure S6L). These findings are consistent with a model in which PARP1-mediated recruitment of CHD2 triggers localized chromatin remodeling that promotes the efficient assembly of NHEJ complexes.

PARP1 and CHD2 Link Histone H3.3 to NHEJ

To further probe into possible mechanisms that underlie CHD2's ability to promote NHEJ, we turned our attention to histone variant H3.3. Recent studies revealed that CHD2 associates with H3.3 and incorporates this variant at sites of transcription (Harada et al., 2012; Siggens et al., 2015). Moreover, H3.3 is also incorporated at sites of UV-C-induced DNA damage (Adam et al., 2013). To confirm the interaction between these proteins, we performed coIP experiments, which indeed showed a robust interaction between endogenous CHD2 and H3.3 (Figure 7A). Prompted by these findings, we sought to address whether CHD2 also cooperates with H3.3 in DSB repair. To study this, we generated cells stably expressing low levels of SNAP-tagged H3.3, which allows the fluorescent labeling and monitoring of newly synthesized histone H3.3 (Adam et al., 2013) (Figure 7B; Figure S7A). Local micro-irradiation revealed the rapid deposition of H3.3 at sites of DSBs within several minutes after damage induction, which was severely reduced in CHD2-depleted cells (Figures 7C and 7D). Similarly, overexpression of ATPase-dead CHD2 (K515R; Figure S5F), but not wild-type CHD2, significantly reduced H3.3 deposition (Figure 7E), suggesting that CHD2's chromatin remodeling activity contributes to H3.3 assembly at DSBs. Incorporation of H3.1 could also be detected, albeit much weaker than the H3.3 assembly (Figure S7B). Importantly, deposition of H3.3 only occurred following micro-irradiation of cells that were pre-sensitized with BrdU, showing that not the UV-A irradiation itself, but rather the generation of laser-induced DSBs caused by BrdU sensitization triggers this response (Figure S7C) (Limoli and Ward, 1993). Considering that CHD2 recruitment is mediated by PARP1, we next addressed if PARP1 is involved in H3.3 deposition. CoIP experiments revealed an interaction between H3.3 and PARP1, which was not enhanced by DNA damage induction (Figure 7F). Importantly, treatment of cells with PARP inhibitor or siRNA-mediated depletion of PARP1 significantly reduced the de novo incorporation of H3.3 at DSBs (Figures 7G and 7H; Figures S7D–S7F). To analyze if H3.3 is required for DSB repair, we transfected siRNAs targeting both H3.3 genes in human cells, which efficiently depleted H3.3 (Figure 7I) without affecting cell

Figure 5. CHD2 Promotes the Assembly of NHEJ Complexes at DSBs

(A) Reciprocal coIPs of endogenous CHD2 and KU70 in HEK293 cells.

(B) Recruitment of GFP-KU70 to multi-photon tracks in HeLa cells.

(C) As in (B), except for GFP-XRCC4 in U2OS cells.

(D) siRNA-transfected pTuner265 cells were induced for FokI-LacR expression and stained for γH2AX and XRCC4.

(E) U2OS cells transfected with the indicated constructs were UV-A micro-irradiated and stained for γH2AX and XRCC4.

(F and G) Recruitment kinetics of GFP-XRCC4 to multi-photon tracks in (F) U2OS cells treated with DMSO or 10 μM PARPi or in (G) U2OS cells transfected with the indicated siRNAs. 40–160 cells were analyzed from (B) three or (C–E) two independent experiments.

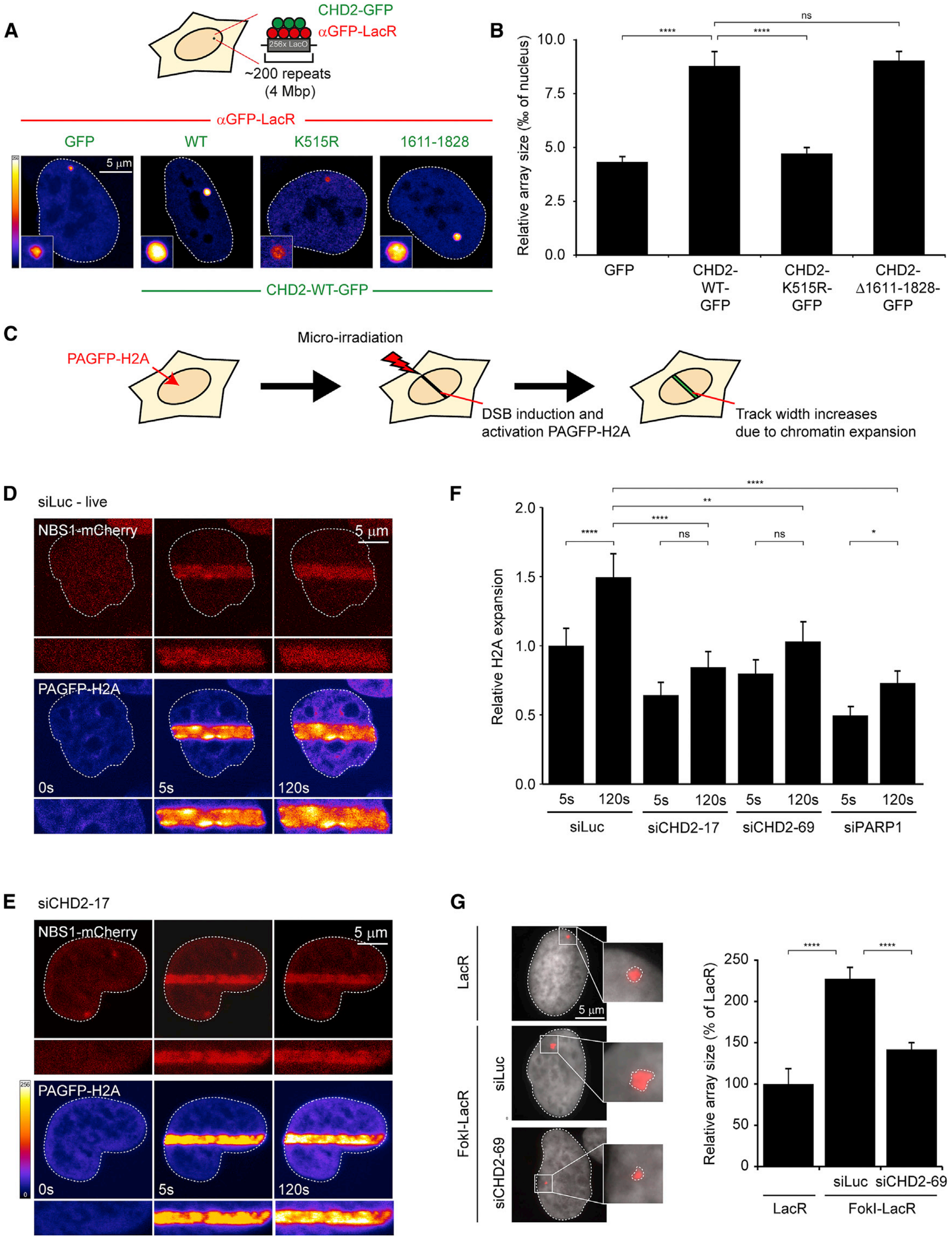

Figure 6. CHD2 Promotes DNA Damage-Induced Chromatin Changes

(A) U2OS 2-6-3 cells containing a LacO array were co-transfected with αGFP-mCherry-LacR and GFP-tagged CHD2 variants or GFP only.

(B) Quantification of the array size upon tethering of the indicated proteins.

(C) Outline of the PAGFP-H2A expansion approach.

(D and E) PAGFP-H2A expansion in U2OS cells transfected with the indicated siRNAs. NBS1-mCherry was a DNA damage marker.

(F) Quantification of the PAGFP-H2A expansion experiments. Values were corrected for the expansion in fixed cells and normalized to 1 for siLuc at 5 s post irradiation.

(G) U2OS 2-6-3 cells were transfected with mCherry-LacR, whereas 2-6-3-derived pTuner265 cells were transfected with the indicated siRNAs and induced for FokI-LacR expression. 60–100 cells were analyzed from (B and F) three or (G) two independent experiments.

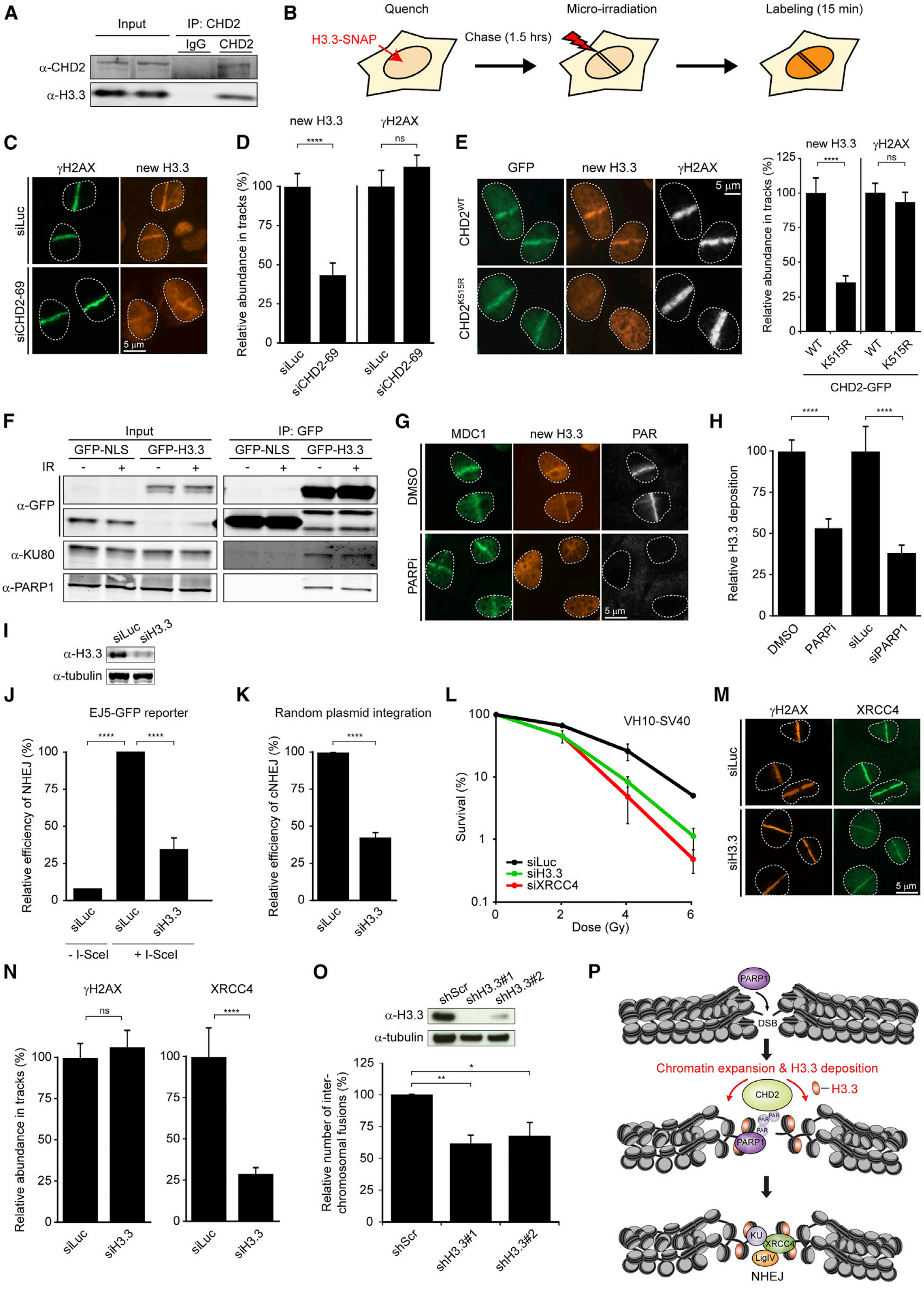

Figure 7. CHD2-Mediated H3.3 Deposition Regulates NHEJ

(A) CoIP of endogenous CHD2 and H3.3 in HEK293 cells.

(B) Outline of the H3.3 deposition approach.

(C) Deposition of H3.3 at UV-A tracks in U2OS cells transfected with the indicated siRNAs.

(legend continued on next page)

cycle progression (Figure S7G) or the steady-state levels of PARP1 and core NHEJ proteins (Figure S7H). Knockdown of H3.3 caused a severe reduction in NHEJ activity as measured by the EJ5-GFP reporter (Figure 7J) and the plasmid integration assay (Figure 7K). In addition, it also moderately reduced aNHEJ (Figures S7I and S7J) and HR (Figures S7K and S7L), the latter of which agrees with a published report (Yang et al., 2013). Consistent with a defect in DSB repair, we found that loss of H3.3 rendered VH10-SV40 and U2OS cells highly sensitive to IR (Figure 7L; Figure S7M). Notably, knockdown of H3.3 did not affect CHD2 recruitment (Figures S7N–S7P), in agreement with the notion that PARP1 and CHD2 act upstream of H3.3. Depletion of H3.3 also did not affect PAGFP-H2A dynamics (Figures S6K and S7L), suggesting that CHD2-mediated chromatin expansion precedes H3.3 deposition. Similar to CHD2, coIP experiments revealed that H3.3 interacts with a member of the KU complex (KU80; Figure 7F). Moreover, just like depletion of PARP1 or CHD2, depletion of H3.3 severely reduced the KU-dependent assembly of XRCC4 in damaged chromatin (Figures 7M, and7N). To test if H3.3, similar to CHD2, affects NHEJ-dependent chromosome-end fusions (Figures 4F–4I), we simultaneously knocked down both H3.3 genes in mouse TRF2^{ts} cells and induced telomere uncapping. Strikingly, knockdown of H3.3 by two combinations of shRNAs significantly reduced interchromosomal end fusions (Figure 7O). These findings suggest that both CHD2 and H3.3 promote NHEJ-driven chromosome fusion at uncapped telomeres. In summary, our findings suggest that the recruitment of CHD2 by PARP1 triggers the assembly of H3.3 at sites of DNA damage creating an accessible chromatin micro-environment that is amenable for DSB repair by NHEJ (Figure 7P).

DISCUSSION

In this study, we established that DSB-containing chromatin undergoes a rapid PARP1-dependent expansion, which coincides with the spreading and efficient recruitment of NHEJ factor XRCC4. The poorly characterized chromatin remodeler CHD2 is the effector of PARP1 in this process and is required for DNA damage-induced chromatin expansion, the DNA damage-induced deposition of histone variant H3.3, and the efficient recruitment and functioning of NHEJ repair complexes.

CHD2 Promotes cNHEJ

Initial studies have revealed that chromatin containing DSBs undergoes rapid ATP-dependent expansion (Kruhlak et al., 2006). We and others have recently shown that these chromatin changes rely on the activity of PARP enzymes (Khurana et al., 2014; Smeenk et al., 2013). Our current findings shed light on the underlying molecular mechanism by showing that CHD2 associates with PARP1-generated PAR chains through its C terminus and subsequently promotes DNA damage-induced chromatin expansion. Knockdown of PARP1 or CHD2 significantly reduces, but does not completely abolish chromatin expansion, suggesting that other mechanisms may also contribute to this phenomenon. Although local irradiation of cells using laser micro-irradiation produces different types of DNA lesions, including DSBs and single-stranded breaks, our results suggest that the CHD2-dependent chromatin response requires the presence of DSBs. First, we show that significant chromatin expansion is only observed when using laser conditions that trigger accrual of the DSB repair factor XRCC4. Second, we show that CHD2 promotes the recruitment of the KU complex and XRCC4, both of which respond specifically to DSBs. Third, we find that CHD2 is required for NHEJ-dependent repair of the EJ5-GFP reporter and genomic integration of linearized plasmid DNA. Both of these substrates contain bona fide DSBs generated by endonucleases, and we show that processing of the latter substrate is strictly dependent on canonical NHEJ. Fourth, we find that CHD2 promotes XRCC4 recruitment and chromatin expansion in chromatin surrounding nuclease-induced DSBs. Fifth, and finally, we show in mouse cells that the cNHEJ-dependent fusion of chromosomes containing uncapped telomeres requires the activity of CHD2. Together, these findings argue that the chromatin response mediated by CHD2 is triggered by the presence of DSBs and promotes repair of these lesions by the canonical KU-dependent NHEJ pathway.

PARP1 Contributes to cNHEJ

Our findings reveal that CHD2 is recruited to sites of DNA damage by PARP1 and promotes NHEJ. This raises the question: Is the PARP1-dependent recruitment of CHD2 required for NHEJ? The current view on NHEJ mechanisms distinguishes a fast KU-dependent cNHEJ pathway from a slower PARP1-dependent aNHEJ mechanism (Audebert et al., 2004; Wang et al., 2006). However, the demonstrated role of PARP1 in aNHEJ does not

---

(D) Quantification of (C).

(E) U2OS H3.3-SNAP cells transfected with the indicated GFP constructs were UV-A micro-irradiated, SNAP-labeled, and stained for γH2AX.

(F) CoIP of GFP-H3.3 and KU80 or PARP1 in U2OS cells.

(G) Deposition of H3.3 at UV-A tracks in U2OS cells treated with DMSO or 10 μM PARPi.

(H) Quantification of (G) and of cells transfected with PARP1 siRNAs.

(I) Western blot showing H3.3 knockdown efficiency in U2OS cells.

(J) Quantification of GFP-positive EJ5-GFP HEK293 cells corrected for I-SceI transfection efficiency by co-transfection with mCherry. The average of two independent experiments is shown.

(K) Plasmid integration assay after H3.3 knockdown in U2OS cells. The average of two independent experiments is shown.

(L) Clonogenic survival after IR exposure of siRNA-transfected VH10-SV40 cells.

(M) XRCC4 recruitment to UV-A tracks in siRNA-transfected U2OS cells.

(N) Quantification of (M). 45–100 cells were analyzed from (E) two or (D and H) three independent experiments.

(O) Quantification of interchromosomal fusions observed in shRNA-transduced TRF2^{ts} MEFs after telomere uncapping. 3,200–4,600 chromosomes were analyzed from two independent experiments. Western blot showing H3.3 knockdown efficiency.

(P) Model for how PARP1 links CHD2-mediated chromatin expansion and H3.3 assembly to DSB repair by NHEJ.

exclude a role for PARP1 in cNHEJ. Indeed, several studies have implicated PARP1 in cNHEJ, but its contribution is less clear due to conflicting results (reviewed in Pines et al., 2013). We provide evidence for a role of PARP1 in modulating the efficiency of cNHEJ in human cells. First, we show that both the inhibition and knockdown of PARP1 in human cells significantly reduces the assembly of XRCC4 to laser-induced DSBs. Second, we find that knockdown of PARP1 in human cells reduces the cNHEJ-dependent integration of linearized plasmid DNA. These findings suggest that PARP1 is not essential for cNHEJ, but together with CHD2 it promotes the efficiency of this DSB repair pathway in a chromatin environment.

PARP1 Activation in the Presence of KU

Biochemical evidence suggests that KU and PARP1 compete for the binding to broken DNA ends (Cheng et al., 2011; Wang et al., 2006), raising the question: How does PARP1 stimulate cNHEJ in the presence of functional KU? Interestingly, KU limits but does not prevent PARP1 recruitment to DSBs (Cheng et al., 2011). Moreover, live-cell imaging revealed that KU dimers exchange rapidly from DNA ends with a $t_{1/2}$ of 2 min (Mari et al., 2006). This suggests that PARP1 could associate with DSBs recently vacated by KU. Another possibility is that PARP1 associates with DSBs that are not bound by KU and, through CHD2 recruitment, creates a local chromatin environment that promotes the assembly of NHEJ complexes in trans. Either way, our findings support a model in which PARP1 acts upon DSBs in the presence of KU and contributes to DSB repair by cNHEJ. Recent findings have shown that PARP3 also promotes cNHEJ, suggesting that PARP3 can also associate with DSBs in the presence of functional KU (Rulten et al., 2011). How PARP1 and PARP3 cooperate at DSBs is not clear, but the finding that the combined loss of PARP1 and PARP3 renders mice sensitive to IR beyond the impact of the single disruption of either gene, suggests a functional synergy between these PARP enzymes in the DSBs response (Boehler et al., 2011).

CHD2 Contains a PAR-Binding Domain

Our findings link PARP1-mediated PAR synthesis to the recruitment of CHD2. Surprisingly, although CHD2 contains a putative PAR-binding domain (Gagné et al., 2008), we found this domain to be dispensable for DNA damage recruitment. Instead, we identified a C-terminal region located between amino acids 1611 and 1828 to be essential for in vitro PAR binding and the localization of CHD2 at laser-induced DSBs. Interestingly, a heterozygous CHD2 mutant mouse was generated by gene trapping, which expresses a truncated CHD2-β-gal-neomycin fusion protein that contains the first 1198 amino acids of the wild-type protein. Notably, CHD2 gene-trap mice develop lymphomas, and cells from these mice display signs of defective DSB repair (Nagarajan et al., 2009). However, it is unclear whether these phenotypes are caused by a gain-of-function feature of the CHD2 fusion protein or through a loss-of-function feature of CHD2. Using siRNA- and shRNA-mediated knockdown of CHD2 in human and mouse cells, our results provide direct evidence for a role of CHD2 in DSB repair by KU-dependent NHEJ. It is tempting to speculate that the gene-trap allele, which produces a truncated CHD2 protein (CHD2$^{1-1198}$) lacking the C-terminal PAR-binding region, is not functional due to its inability to associate with PAR chains. This region of CHD2 bears no similarity to other known PAR-binding domains, and it would be interesting to biochemically define how it interacts with PAR chains and whether interactions with PAR stimulate the ATPase activity of CHD2.

A Pathway that Regulates NHEJ in Chromatin

How does the PARP1-dependent recruitment of CHD2 promote NHEJ? Our data reveal that, similar to transcription sites (Harada et al., 2012; Siggens et al., 2015), the deposition of H3.3 at DSBs is regulated by CHD2's chromatin remodeling activity. However, whether CHD2 directly deposits H3.3, as was demonstrated in vitro for the p400 ATPase (Pradhan et al., 2016), or if it cooperates with known H3.3 chaperones remains to be investigated (Adam et al., 2013). Knockdown of H3.3, like knockdown of CHD2, results in a profound defect in DSB repair by NHEJ, suggesting that CHD2 promotes NHEJ, at least in part, through the DNA damage-dependent assembly of H3.3. The deposition of H3.3 may create a chromatin environment that facilitates the assembly of functional NHEJ complexes, and this process may be aided by interactions between H3.3 and the KU complex. Interestingly, somatic mutations in CHD2 and H3.3 genes have been found to drive tumorigenesis (Rodríguez et al., 2015; Yuen and Knoepfler, 2013), suggesting that the uncovered pathway may contribute to tumor suppression by maintaining genetic stability. In summary, we define a pathway involved in facilitating NHEJ in a chromatin context. Our findings support a model in which PARP1-associated PAR chains attract the chromatin-remodeling activity of CHD2 to deposit histone variant H3.3 and generate an accessible chromatin environment that promotes the efficient assembly of NHEJ complexes at DSBs. In addition to its described role in aNHEJ, PARP1 also contributes to efficient KU-dependent cNHEJ in human cells through its effectors CHD2 and H3.3. The strong link between these factors raises the question whether CHD2 and H3.3 play a role in other genome maintenance pathways that are modulated by PARP1 (Pines et al., 2013).

EXPERIMENTAL PROCEDURES

Cell Lines, Chemicals, Plasmids, and Transfections

Cells (see the Supplemental Information) were cultured in DMEM, supplemented with antibiotics and 10% fetal calf serum. PARP inhibitor (KU-0058948) was used at a concentration of 1–10 μM. The CHD2 cDNA was inserted into pEGFP-N1 (Addgene). All indicated deletion mutants of CHD2 were generated by PCR. Plasmid DNA or siRNAs were transfected using Lipofectamine 2000 or RNAiMAX (Invitrogen). See the Supplemental Information for details on siRNAs, shRNAs, and primers.

Immunoprecipitation for Mass Spectrometry and PAR-Binding Assay

GFP-tagged PARP1 and CHD2 were immunoprecipitated, trypsinized, desalted, and analyzed on a Q-Exactive Orbitrap mass spectrometer (Thermo Scientific, Germany) coupled to an EASY-nanoLC 1000 system (Proxeon, Odense, Denmark). CHD2-GFP fragments were immunoprecipitated, separated by SDS-PAGE, and incubated with radioactive PAR. Radioactivity was detected by a phosphor-imager screen.

Microscopic Analysis

Laser micro-irradiation was performed by UV-A micro-irradiation of BrdU-sensitized cells or by multi-photon (MP) irradiation using a titanium-sapphire laser. PAGFP-H2A was photoactivated using the same MP laser and settings as those used to inflict localized DNA damage (see the Supplemental Information for details). Immunostaining was performed as described (Luijsterburg et al., 2012a). Primary antibodies are listed in the Supplemental Information.

H3.3-SNAP Labeling

U2OS H3.3-SNAP cells were blocked with SNAP-Cell Block (New England Biolabs), subjected to UV-A micro-irradiation after which newly synthesized histones were labeled with SNAP-cell TMR star (New England Biolabs).

DSB Repair Assays

EJ5-GFP, EJ2-GFP, and DR-GFP reporter assays were carried out as described previously (Smeenk et al., 2013). Gel-purified BamHI-EcoRI-linearized pEGFP-C1 plasmid was transfected into siRNA-depleted cells to measure random plasmid integration events (see the Supplemental Information) (Galanty et al., 2009).

Chromosome Fusion Assays

TRF2^{ts} MEFs were infected with shRNAs constructs and shifted to the non-permissive temperature (39°C) for 24 hr to induce telomere uncapping followed by telomere-FISH, as described (Boersma et al., 2015).

Statistical Analysis

Statistical significance was assessed by a two-tailed, unpaired t test and is indicated as follows: ****$p < 0.0001$, ***$p < 0.001$, **$p < 0.01$, and *$p < 0.05$. ns, not significant. All error bars represent the SEM.

SUPPLEMENTAL INFORMATION

Supplemental Information includes Supplemental Experimental Procedures, seven figures, and one table and can be found with this article online at http://dx.doi.org/10.1016/j.molcel.2016.01.019.

AUTHOR CONTRIBUTIONS

M.S.L. generated constructs and stable cell lines; performed micro-irradiation and photo-activation experiments, LacR-based tethering assays, H3.3 deposition assays, and IPs for mass spectrometry; and wrote the paper. W.W.W. performed multi-photon and photo-activation experiments, clonogenic survivals, plasmid integration assays, coIPs, and DR-GFP, EJ5-GFP, and EJ2-GFP reporter assays. G.S. performed clonogenic survivals using shRNAs and siRNA as well as the EJ5-GFP reporter assay. A.J.L.d.G. performed CHD2 coIPs. A.J.L.d.G. and A.P. performed coIPs for mass spectrometry. A.P. and A.C.O.V. analyzed the mass spectrometry samples. R.G.S. and G.M.S. performed PARP1 coIPs and in vitro PAR-binding assays. I.d.K. and J.J.L.J. performed the telomere uncapping and chromosome fusion analysis. H.v.A. supervised the project and wrote the paper.

ACKNOWLEDGMENTS

The authors acknowledge Jer-Gung Chang, Remco Derr, Jiabo Di, and Pierre Caron for valuable support and Penny Jeggo, Heinrich Leonardt, and Michael Hendzel for providing cDNA constructs. Dik van Gent, Mauro Modesti, Maria Jasin, and Jeremy Stark generously provided cell lines and reagents. We acknowledge Natalia Lukashchuk and Stephen Jackson for advice regarding the plasmid integration assay. This work was funded by a FEBS fellowship, LUMC research fellowship, and an NWO-VENI grant to M.S.L., an ERC Starting grant to A.C.O.V., an ERC Starting grant and an EMBO Young Investigator Award to J.J.L.J., a Discovery Grant from the Natural Sciences and Engineering Research Council of Canada to G.M.S., and an ERC Consolidator grant to H.v.A. M.S.L. and H.v.A. also acknowledge the Bontius Stichting for financial support.

Received: July 17, 2015
Revised: November 16, 2015
Accepted: January 15, 2016
Published: February 18, 2016

REFERENCES

Adam, S., Polo, S.E., and Almouzni, G. (2013). Transcription recovery after DNA damage requires chromatin priming by the H3.3 histone chaperone HIRA. Cell *155*, 94–106.

Audebert, M., Salles, B., and Calsou, P. (2004). Involvement of poly(ADP-ribose) polymerase-1 and XRCC1/DNA ligase III in an alternative route for DNA double-strand breaks rejoining. J. Biol. Chem. *279*, 55117–55126.

Bennardo, N., Cheng, A., Huang, N., and Stark, J.M. (2008). Alternative-NHEJ is a mechanistically distinct pathway of mammalian chromosome break repair. PLoS Genet. *4*, e1000110.

Boehler, C., Gauthier, L.R., Mortusewicz, O., Biard, D.S., Saliou, J.M., Bresson, A., Sanglier-Cianferani, S., Smith, S., Schreiber, V., Boussin, F., and Dantzer, F. (2011). Poly(ADP-ribose) polymerase 3 (PARP3), a newcomer in cellular response to DNA damage and mitotic progression. Proc. Natl. Acad. Sci. USA *108*, 2783–2788.

Boersma, V., Moatti, N., Segura-Bayona, S., Peuscher, M.H., van der Torre, J., Wevers, B.A., Orthwein, A., Durocher, D., and Jacobs, J.J. (2015). MAD2L2 controls DNA repair at telomeres and DNA breaks by inhibiting 5′ end resection. Nature *521*, 537–540.

Burgess, R.C., Burman, B., Kruhlak, M.J., and Misteli, T. (2014). Activation of DNA damage response signaling by condensed chromatin. Cell Rep. *9*, 1703–1717.

Cheng, Q., Barboule, N., Frit, P., Gomez, D., Bombarde, O., Couderc, B., Ren, G.S., Salles, B., and Calsou, P. (2011). Ku counteracts mobilization of PARP1 and MRN in chromatin damaged with DNA double-strand breaks. Nucleic Acids Res. *39*, 9605–9619.

Gagné, J.P., Isabelle, M., Lo, K.S., Bourassa, S., Hendzel, M.J., Dawson, V.L., Dawson, T.M., and Poirier, G.G. (2008). Proteome-wide identification of poly(ADP-ribose) binding proteins and poly(ADP-ribose)-associated protein complexes. Nucleic Acids Res. *36*, 6959–6976.

Galanty, Y., Belotserkovskaya, R., Coates, J., Polo, S., Miller, K.M., and Jackson, S.P. (2009). Mammalian SUMO E3-ligases PIAS1 and PIAS4 promote responses to DNA double-strand breaks. Nature *462*, 935–939.

Harada, A., Okada, S., Konno, D., Odawara, J., Yoshimi, T., Yoshimura, S., Kumamaru, H., Saiwai, H., Tsubota, T., Kurumizaka, H., et al. (2012). Chd2 interacts with H3.3 to determine myogenic cell fate. EMBO J. *31*, 2994–3007.

Ismail, I.H., Gagné, J.P., Caron, M.C., McDonald, D., Xu, Z., Masson, J.Y., Poirier, G.G., and Hendzel, M.J. (2012). CBX4-mediated SUMO modification regulates BMI1 recruitment at sites of DNA damage. Nucleic Acids Res. *40*, 5497–5510.

Khurana, S., Kruhlak, M.J., Kim, J., Tran, A.D., Liu, J., Nyswaner, K., Shi, L., Jailwala, P., Sung, M.H., Hakim, O., and Oberdoerffer, P. (2014). A macrohistone variant links dynamic chromatin compaction to BRCA1-dependent genome maintenance. Cell Rep. *8*, 1049–1062.

Kruhlak, M.J., Celeste, A., Dellaire, G., Fernandez-Capetillo, O., Müller, W.G., McNally, J.G., Bazett-Jones, D.P., and Nussenzweig, A. (2006). Changes in chromatin structure and mobility in living cells at sites of DNA double-strand breaks. J. Cell Biol. *172*, 823–834.

Lieber, M.R. (2010). The mechanism of double-strand DNA break repair by the nonhomologous DNA end-joining pathway. Annu. Rev. Biochem. *79*, 181–211.

Limoli, C.L., and Ward, J.F. (1993). A new method for introducing double-strand breaks into cellular DNA. Radiat. Res. *134*, 160–169.

Luijsterburg, M.S., and van Attikum, H. (2011). Chromatin and the DNA damage response: the cancer connection. Mol. Oncol. *5*, 349–367.

Luijsterburg, M.S., Acs, K., Ackermann, L., Wiegant, W.W., Bekker-Jensen, S., Larsen, D.H., Khanna, K.K., van Attikum, H., Mailand, N., and Dantuma, N.P.

(2012a). A new non-catalytic role for ubiquitin ligase RNF8 in unfolding higher-order chromatin structure. EMBO J. *31*, 2511–2527.

Luijsterburg, M.S., Lindh, M., Acs, K., Vrouwe, M.G., Pines, A., van Attikum, H., Mullenders, L.H., and Dantuma, N.P. (2012b). DDB2 promotes chromatin decondensation at UV-induced DNA damage. J. Cell Biol. *197*, 267–281.

Mari, P.O., Florea, B.I., Persengiev, S.P., Verkaik, N.S., Brüggenwirth, H.T., Modesti, M., Giglia-Mari, G., Bezstarosti, K., Demmers, J.A., Luider, T.M., et al. (2006). Dynamic assembly of end-joining complexes requires interaction between Ku70/80 and XRCC4. Proc. Natl. Acad. Sci. USA *103*, 18597–18602.

Nagarajan, P., Onami, T.M., Rajagopalan, S., Kania, S., Donnell, R., and Venkatachalam, S. (2009). Role of chromodomain helicase DNA-binding protein 2 in DNA damage response signaling and tumorigenesis. Oncogene *28*, 1053–1062.

Pines, A., Mullenders, L.H., van Attikum, H., and Luijsterburg, M.S. (2013). Touching base with PARPs: moonlighting in the repair of UV lesions and double-strand breaks. Trends Biochem. Sci. *38*, 321–330.

Polo, S.E., and Jackson, S.P. (2011). Dynamics of DNA damage response proteins at DNA breaks: a focus on protein modifications. Genes Dev. *25*, 409–433.

Pradhan, S.K., Su, T., Yen, L., Jacquet, K., Huang, C., Cote, J., Kurdistani, S.K., and Carey, M.F. (2016). EP400 deposits H3.3 into promoters and enhancers during gene activation. Mol. Cell *61*, 27–38.

Rodríguez, D., Bretones, G., Quesada, V., Villamor, N., Arango, J.R., López-Guillermo, A., Ramsay, A.J., Baumann, T., Quirós, P.M., Navarro, A., et al. (2015). Mutations in CHD2 cause defective association with active chromatin in chronic lymphocytic leukemia. Blood *126*, 195–202.

Rulten, S.L., Fisher, A.E., Robert, I., Zuma, M.C., Rouleau, M., Ju, L., Poirier, G., Reina-San-Martin, B., and Caldecott, K.W. (2011). PARP-3 and APLF function together to accelerate nonhomologous end-joining. Mol. Cell *41*, 33–45.

Sfeir, A., and de Lange, T. (2012). Removal of shelterin reveals the telomere end-protection problem. Science *336*, 593–597.

Siggens, L., Cordeddu, L., Rönnerblad, M., Lennartsson, A., and Ekwall, K. (2015). Transcription-coupled recruitment of human CHD1 and CHD2 influences chromatin accessibility and histone H3 and H3.3 occupancy at active chromatin regions. Epigenetics Chromatin *8*, 4.

Smeenk, G., and van Attikum, H. (2013). The chromatin response to DNA breaks: leaving a mark on genome integrity. Annu. Rev. Biochem. *82*, 55–80.

Smeenk, G., Wiegant, W.W., Marteijn, J.A., Luijsterburg, M.S., Sroczynski, N., Costelloe, T., Romeijn, R.J., Pastink, A., Mailand, N., Vermeulen, W., and van Attikum, H. (2013). Poly(ADP-ribosyl)ation links the chromatin remodeler SMARCA5/SNF2H to RNF168-dependent DNA damage signaling. J. Cell Sci. *126*, 889–903.

Smogorzewska, A., Karlseder, J., Holtgreve-Grez, H., Jauch, A., and de Lange, T. (2002). DNA ligase IV-dependent NHEJ of deprotected mammalian telomeres in G1 and G2. Curr. Biol. *12*, 1635–1644.

Symington, L.S., and Gautier, J. (2011). Double-strand break end resection and repair pathway choice. Annu. Rev. Genet. *45*, 247–271.

Wang, M., Wu, W., Wu, W., Rosidi, B., Zhang, L., Wang, H., and Iliakis, G. (2006). PARP-1 and Ku compete for repair of DNA double strand breaks by distinct NHEJ pathways. Nucleic Acids Res. *34*, 6170–6182.

Yang, X., Li, L., Liang, J., Shi, L., Yang, J., Yi, X., Zhang, D., Han, X., Yu, N., and Shang, Y. (2013). Histone acetyltransferase 1 promotes homologous recombination in DNA repair by facilitating histone turnover. J. Biol. Chem. *288*, 18271–18282.

Yuen, B.T., and Knoepfler, P.S. (2013). Histone H3.3 mutations: a variant path to cancer. Cancer Cell *24*, 567–574.

Molecular Cell, Volume *61*

Supplemental Information

PARP1 Links CHD2-Mediated Chromatin Expansion and H3.3 Deposition to DNA Repair by Non-homologous End-Joining

Martijn S. Luijsterburg, Inge de Krijger, Wouter W. Wiegant, Rashmi G. Shah, Godelieve Smeenk, Anton J.L. de Groot, Alex Pines, Alfred C.O. Vertegaal, Jacqueline J.L. Jacobs, Girish M. Shah, and Haico van Attikum

Figure S1

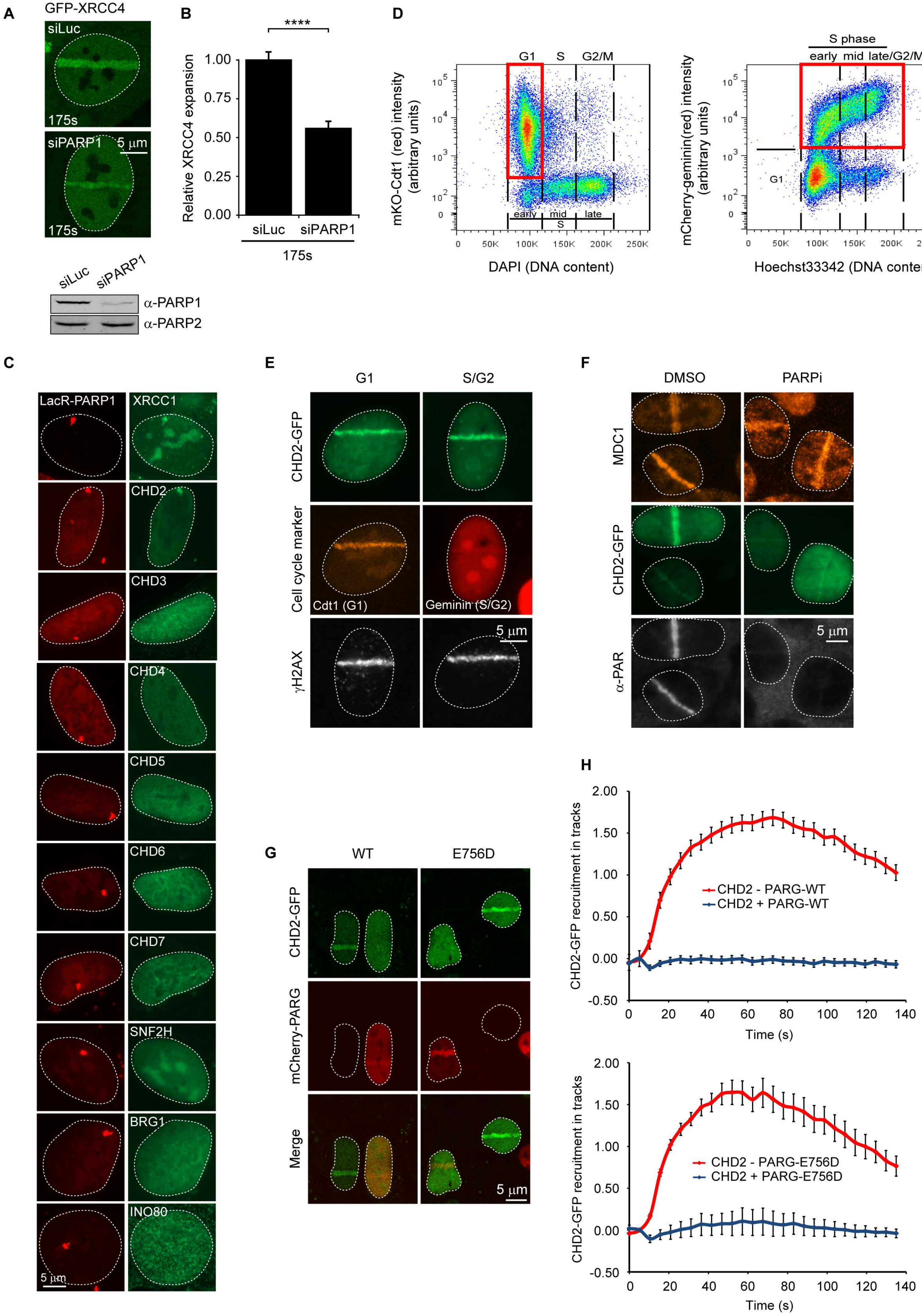
A
GFP-XRCC4
siLuc
175s
siPARP1
5 µm
175s
siLuc
siPARP1
α-PARP1
α-PARP2
B
****
Relative XRCC4 expansion
1.00
0.75
0.50
0.25
0.00
siLuc
siPARP1
175s
D
G1
S
G2/M
mKO-Cdt1 (red) intensity (arbitrary units)
10^5
10^4
10^3
10^2
0
early
mid
late
S
0
50K
100K
150K
200K
250K
DAPI (DNA content)
S phase
early
mid
late/G2/M
mCherry-geminin(red) intensity (arbitrary units)
G1
Hoechst33342 (DNA content)
C
LacR-PARP1
XRCC1
CHD2
CHD3
CHD4
CHD5
CHD6
CHD7
SNF2H
BRG1
INO80
5 µm
E
G1
S/G2
CHD2-GFP
Cell cycle marker
Cdt1 (G1)
Geminin (S/G2)
γH2AX
5 µm
F
DMSO
PARPi
MDC1
CHD2-GFP
α-PAR
5 µm
G
WT
E756D
CHD2-GFP
mCherry-PARG
Merge
5 µm
H
CHD2-GFP recruitment in tracks
2.00
1.50
1.00
0.50
0.00
-0.50
CHD2 - PARG-WT
CHD2 + PARG-WT
0
20
40
60
80
100
120
140
Time (s)
CHD2 - PARG-E756D
CHD2 + PARG-E756D
Time (s)

Figure S1. Screen for PARP1-interacting chromatin remodelers. Related to Figure 1 and 2. (A) Expansion of GFP-XRCC4 tracks in U2OS cells transfected with PARP1 siRNAs (upper panel). Western blot showing PARP1 knockdown efficiency for the indicated siRNA (lower panel). PARP2 is a loading control. (B) Quantification of XRCC4 track expansion shown in A. 24-28 cells were analysed from 2 independent experiments. (C) U2OS 2-6-3 cells harbouring a LacO array were transfected with mCherry-LacR-PARP1 and the indicated epitope-tagged ATPases from the four major families (CHD, SWI/SNF, ISWI, INO80) of chromatin remodellers. All indicated proteins were tagged with GFP, expect for CHD3 and INO80, which were tagged with FLAG. GFP-XRCC1 is a positive control. (D) Validation of mKO-Cdt1 and mCherry-geminin cells by FACS-based cell cycle analysis. Identification of mKO-Cdt1-positive G1 and mCherry-geminin-positive S/G2 cells is shown for the respective cell lines. (E) U2OS cells expressing mKO-Cdt1 (G1 marker) or mCherry-geminin (S/G2 marker) were transfected with CHD2-GFP, UV-A micro-irradiated and stained for γH2AX. (F) U2OS cells expressing CHD2-GFP were treated with either DMSO or PARPi, micro-irradiated and stained for MDC1 and PAR chains. (G) Live cell imaging of stable CHD2-GFP cells that were transfected with mCherry-tagged PARP (WT or E756D) and subjected to multiphoton micro-irradiation. (H) Quantification of G. 20-30 cells were analysed from 2 independent experiments. Error bars represent the SEM. Statistical significance based on a two-tailed, unpaired t-test is indicated as: ****$p < 0.0001$, ***$p < 0.001$, **$p < 0.01$, *$p < 0.05$. ns, not significant.

Figure S2

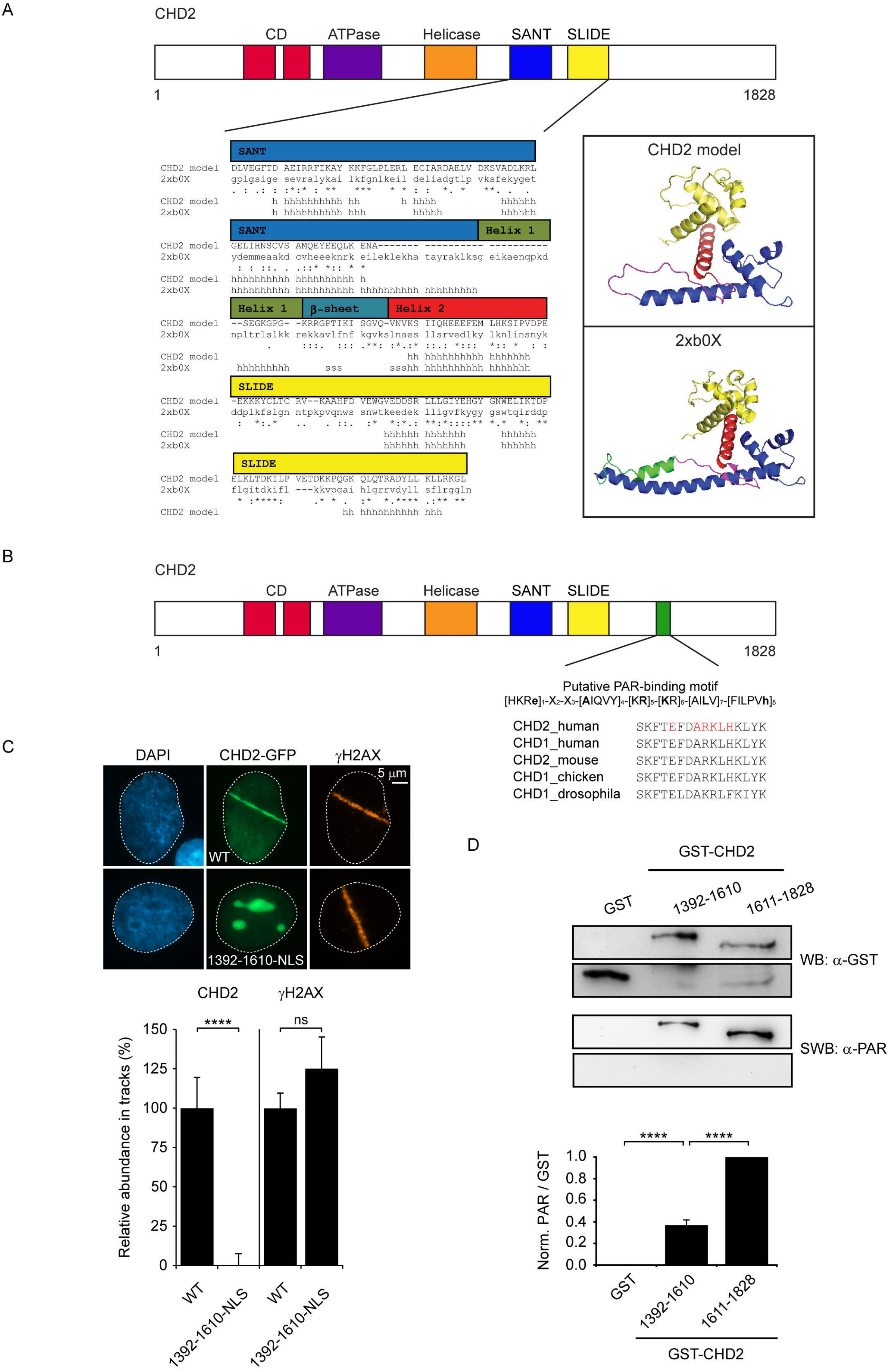

```
              SANT
CHD2 model    DLVEGFTD AEIRRFIKAY KKFGLPLERL ECIARDAELV DKSVADLKRL
2xb0X         gplgsige sevralykai lkfgnlkeil deliadgtlp vksfekyget
              . : .: : :*:* : **   ***   * * : :  *. *   **. .  .
CHD2 model           h hhhhhhhhhh hh       h hhhh           hhhhhh
2xb0X                h hhhhhhhhhh hhh        hhhhh          hhhhhh
              SANT                                         Helix 1
CHD2 model    GELIHNSCVS AMQEYEEQLK ENA------- ---------- ----------
2xb0X         ydemmeaakd cvheeeknrk eileklekha tayraklksg eikaenqpkd
               : : ::. . .::* *:: * *
CHD2 model    hhhhhhhhhh hhhhhhhhhh h
2xb0X         hhhhhhhhhh hhhhhhhhhh hhhhhhhhhh hhhhhhhhh
              Helix 1     β-sheet     Helix 2
CHD2 model    --SEGKGPG- -KRRGPTIKI SGVQ-VNVKS IIQHEEEFEM LHKSIPVDPE
2xb0X         npltrlslkk rekkavlfnf kgvkslnaes llsrvedlky lknlinsnyk
                    .     :::.  ::: .**: :*.:* ::.: *:::  *:: *  : :
CHD2 model                                  hh hhhhhhhhhh hhhhhhh
2xb0X          hhhhhhhhh      sss        ssshh hhhhhhhhhh hhhhhhh
              SLIDE
CHD2 model    -EKKKYCLTC RV--KAAHFD VEWGVEDDSR LLLGIYEHGY GNWELIKTDP
2xb0X         ddplkfslgn ntpkpvqnws snwtkeedek lligvfkygy gswtqirddp
               :  *:.*   ..   . ::.  :*  *:*.: **:*::::** *.*  *: **
CHD2 model                              hhhhhh hhhhhhh      hhhhhh
2xb0X                                   hhhhhh hhhhhhh      hhhhhh
              SLIDE
CHD2 model    ELKLTDKILP VETDKKPQGK QLQTRADYLL KLLRKGL
2xb0X         flgitdkifl ---kkvpgai hlgrrvdyll sflrggln
               * :****:     .* * .  :*  *.**** .:** **
CHD2 model                       hh hhhhhhhhhh hhh
```

Putative PAR-binding motif

$[HKRe]_1$-X_2-X_3-$[AIQVY]_4$-$[KR]_5$-$[KR]_6$-$[AILV]_7$-$[FILPVh]_8$

CHD2_human SKFTEFDARKLHKLYK
CHD1_human SKFTEFDARKLHKLYK
CHD2_mouse SKFTEFDARKLHKLYK
CHD1_chicken SKFTEFDARKLHKLYK
CHD1_drosophila SKFTELDAKRLFKIYK

Figure S2. CHD2 contains a putative PAR-binding domain. Related to Figure 3. (A) Schematic representation of the human CHD2 protein and its domains. An amino acid sequence alignment of the putative SANT and SLIDE domains of human CHD2 and the crystallized sequence of yeast CHD1 2xb0X domain are shown (Ryan et al., 2011). Colours reflect those in the structures next to the alignment. A structural model of CHD2 SANT and SLIDE domains and the experimentally determined structure of yeast CHD1 are shown. (B) CHD2 contains a putative PAR-binding domain (green) that almost matches the consensus $[HKRe]_1$-X_2-X_3-$[AIQVY]_4$-$[KR]_5$- $[KR]_6$-$[AILV]_7$-$[FILPVh]_8$ (Gagne et al., 2008) and is conserved between human CHD1 and drosophila CHD1. (C) U2OS cells depleted for endogenous CHD2 were transfected with $CHD2^{WT}$-GFP or $CHD2^{1392\text{-}1610}$-GFP-NLS. Cells were UV-A micro-irradiated and stained for γH2AX. The quantification is shown next to the images. 22-27 cells were analysed from 2 independent experiments. (D) Association of recombinant GST-CHD2 fusion proteins with recombinant PAR was analysed by southwestern blotting. Quantification of PAR binding by the indicated CHD2 fragments. Results from three independent experiments are shown. Error bars represent the SEM. Statistical significance based on a two-tailed, unpaired t-test is indicated as: ****$p < 0.0001$, ***$p < 0.001$, **$p < 0.01$, *$p < 0.05$. ns, not significant.

Figure S3

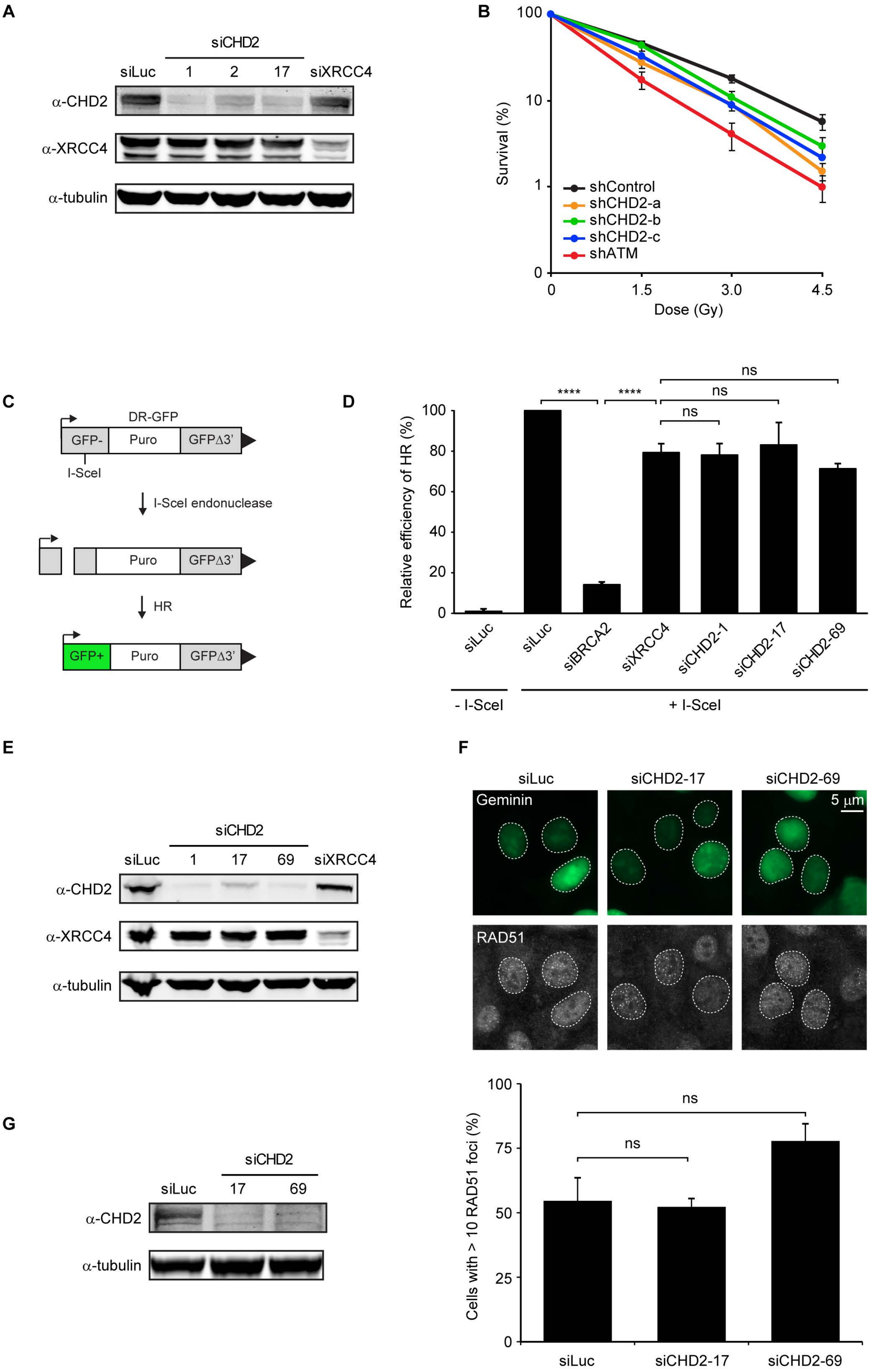
A
siCHD2
siLuc
1
2
17
siXRCC4
α-CHD2
α-XRCC4
α-tubulin
B
100
10
1
0
Survival (%)
shControl
shCHD2-a
shCHD2-b
shCHD2-c
shATM
0
1.5
3.0
4.5
Dose (Gy)
C
DR-GFP
GFP-
Puro
GFPΔ3'
I-SceI
I-SceI endonuclease
Puro
GFPΔ3'
HR
GFP+
Puro
GFPΔ3'
D
Relative efficiency of HR (%)
100
80
60
40
20
0
****
****
ns
ns
ns
siLuc
siLuc
siBRCA2
siXRCC4
siCHD2-1
siCHD2-17
siCHD2-69
- I-SceI
+ I-SceI
E
siCHD2
siLuc
1
17
69
siXRCC4
α-CHD2
α-XRCC4
α-tubulin
F
siLuc
siCHD2-17
siCHD2-69
Geminin
5 μm
RAD51
Cells with > 10 RAD51 foci (%)
100
75
50
25
0
ns
ns
siLuc
siCHD2-17
siCHD2-69
G
siCHD2
siLuc
17
69
α-CHD2
α-tubulin

Figure S3. CHD2 is not required for HR. Related to Figure 4. (A) Knock-down validation for the IR survival shown in **Fig 4A**. (B) Clonogenic survival after X-ray exposure of VH10-hTERT cells stably expressing the indicated shRNAs. (C) Schematic representation of the DR-GFP reporter for HR. (D) HEK293T cells containing the DR-GFP reporter were transfected with the indicated siRNAs and 48 hrs later co-transfected with I-SceI and mCherry expression plasmids. The percentage of GFP/mCherry-positive HEK293 cells was monitored by flow cytometry. The average of 3 experiments is shown. Error bars represent the SEM. (E) Western blot showing CHD2 and XRCC4 knockdown efficiency for the indicated siRNAs in D. (F) U2OS cells stably expressing mAG-geminin (green) were exposed to IR (10 Gy) and after 6 hrs stained for RAD51 (grey). The quantification of geminin-positive cells with more than 10 RAD51 foci is shown below the images. 100-200 cells were analysed from 2 independent experiments. Error bars represent SEM. (G) Western blot showing CHD2 knockdown efficiency for the indicated siRNAs in F. Statistical significance based on a two-tailed, unpaired t-test is indicated as: ****$p < 0.0001$, ***$p < 0.001$, **$p < 0.01$, *$p < 0.05$. ns, not significant.

Figure S4

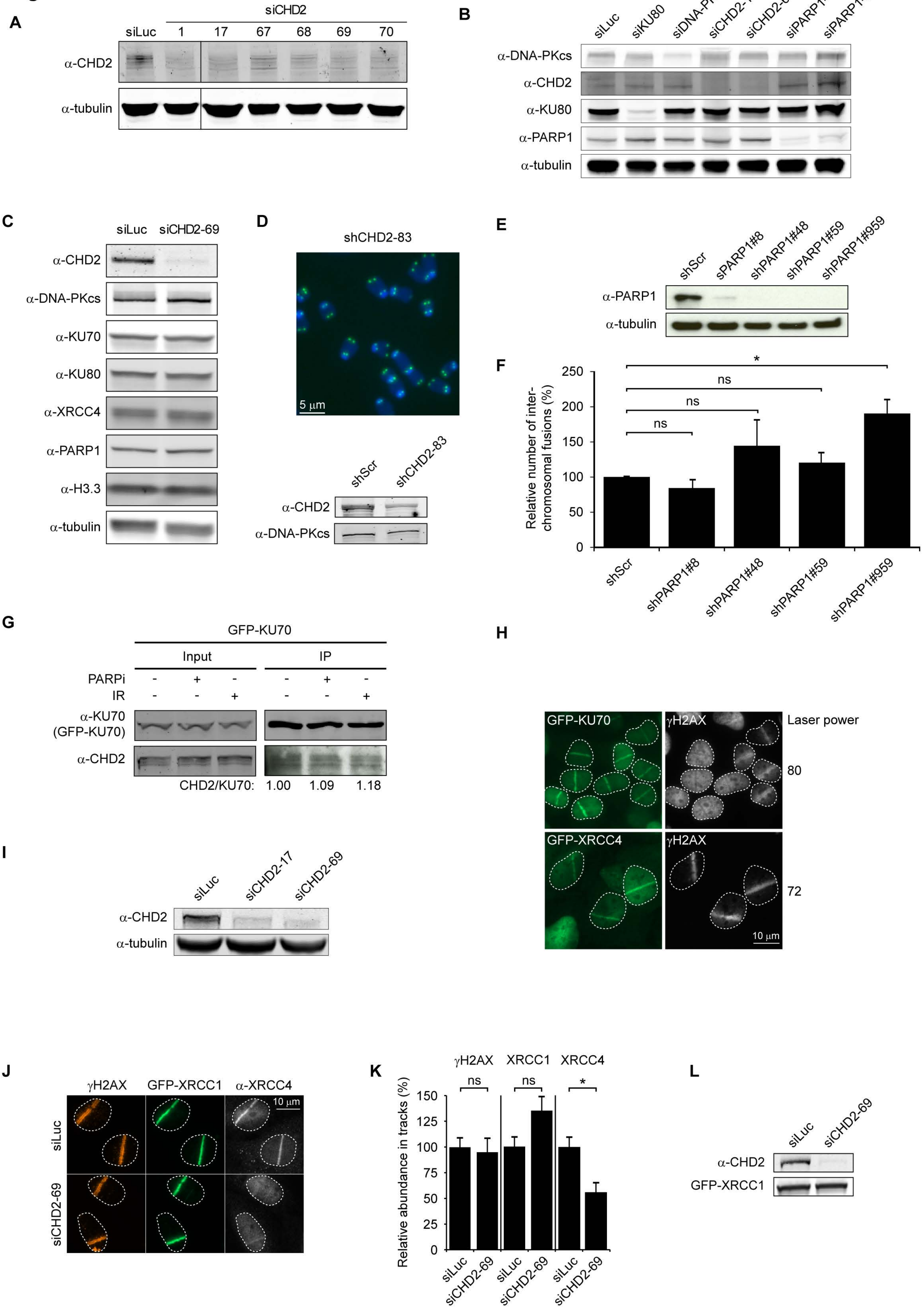
A
siCHD2
siLuc
1
17
67
68
69
70
α-CHD2
α-tubulin
B
siLuc
siKU80
siDNA-PKcs
siCHD2-1
siCHD2-69
siPARP1-1
siPARP1-2
α-DNA-PKcs
α-CHD2
α-KU80
α-PARP1
α-tubulin
C
siLuc
siCHD2-69
α-CHD2
α-DNA-PKcs
α-KU70
α-KU80
α-XRCC4
α-PARP1
α-H3.3
α-tubulin
D
shCHD2-83
5 μm
shScr
shCHD2-83
α-CHD2
α-DNA-PKcs
E
shScr
sPARP1#8
shPARP1#48
shPARP1#59
shPARP1#959
α-PARP1
α-tubulin
F
Relative number of inter-chromosomal fusions (%)
250
200
150
100
50
0
*
ns
ns
ns
shScr
shPARP1#8
shPARP1#48
shPARP1#59
shPARP1#959
G
GFP-KU70
Input
IP
PARPi - + - - + -
IR - - + - - +
α-KU70 (GFP-KU70)
α-CHD2
CHD2/KU70: 1.00 1.09 1.18
H
GFP-KU70
γH2AX
Laser power
80
GFP-XRCC4
γH2AX
72
10 μm
I
siLuc
siCHD2-17
siCHD2-69
α-CHD2
α-tubulin
J
γH2AX
GFP-XRCC1
α-XRCC4
10 μm
siLuc
siCHD2-69
K
γH2AX
XRCC1
XRCC4
ns
ns
*
Relative abundance in tracks (%)
150
125
100
75
50
25
0
siLuc
siCHD2-69
siLuc
siCHD2-69
siLuc
siCHD2-69
L
siLuc
siCHD2-69
α-CHD2
GFP-XRCC1

Figure S4. CHD2 regulates NHEJ. Related to Figure 4 and 5. (A) Western blot showing CHD2 knockdown efficiency for the indicated siRNAs in **Fig 4C**. (B) Western blot showing KU80, DNA-PKcs, CHD2 and PARP1 knockdown efficiency for the indicated siRNAs in **Fig 4E**. (C) Western blot showing that knock-down of CHD2 in U2OS cells does not affect the steady-state levels of NHEJ proteins, PARP1 or H3.3. (D) Representative image of a metaphase from TRF2^{ts} MEFs transduced with the indicated shRNA after 24hrs of telomere uncapping. Telomere-FISH shows the position of the telomeres (green), while chromosomes are stained by DAPI (blue). The western blot shows CHD2 knock-down efficiency for the indicated shRNA. The quantification is shown in **Fig. 4I**. (E) Western blot showing PARP1 knockdown efficiency for the indicated shRNAs in TRF2^{ts} MEFs. (F) Quantification of interchromosomal fusions observed in cells transduced with the indicated shRNAs. Values for cells treated with scrabled control shRNA (shScr) were set to 100%. 1600-3900 chromosomes were analysed from 2-4 independent experiments. Error bars represent the SEM. (G) Co-IP of GFP-KU70 and endogenous CHD2 in U2OS cells that were left untreated or treated with PARP inhibitor (10 µM) or exposure to IR (20 Gy). (H) Accrual of GFP-KU70 or GFP-XRCC4 to sites of UV-A micro-irradiation requires different laser power as indicated by the pan-nuclear or localized appearance of γH2AX. (I) Western blot showing CHD2 knockdown efficiency for the indicated siRNAs in **Fig 5C**. (J) U2OS GFP-XRCC1 cells were transfected with the indicated siRNAs, UV-A micro-irradiated and stained for γH2AX and XRCC4. (K) Quantification of results from J. 25-45 cells were analysed from 2 independent experiments. Error bars represent SEM. (L) Western blot showing CHD2 knockdown efficiency for the indicated siRNA in J. Statistical significance based on a two-tailed, unpaired t-test is indicated as: ****p < 0.0001, ***p < 0.001, **p < 0.01, *p < 0.05. ns, not significant.

Figure S5

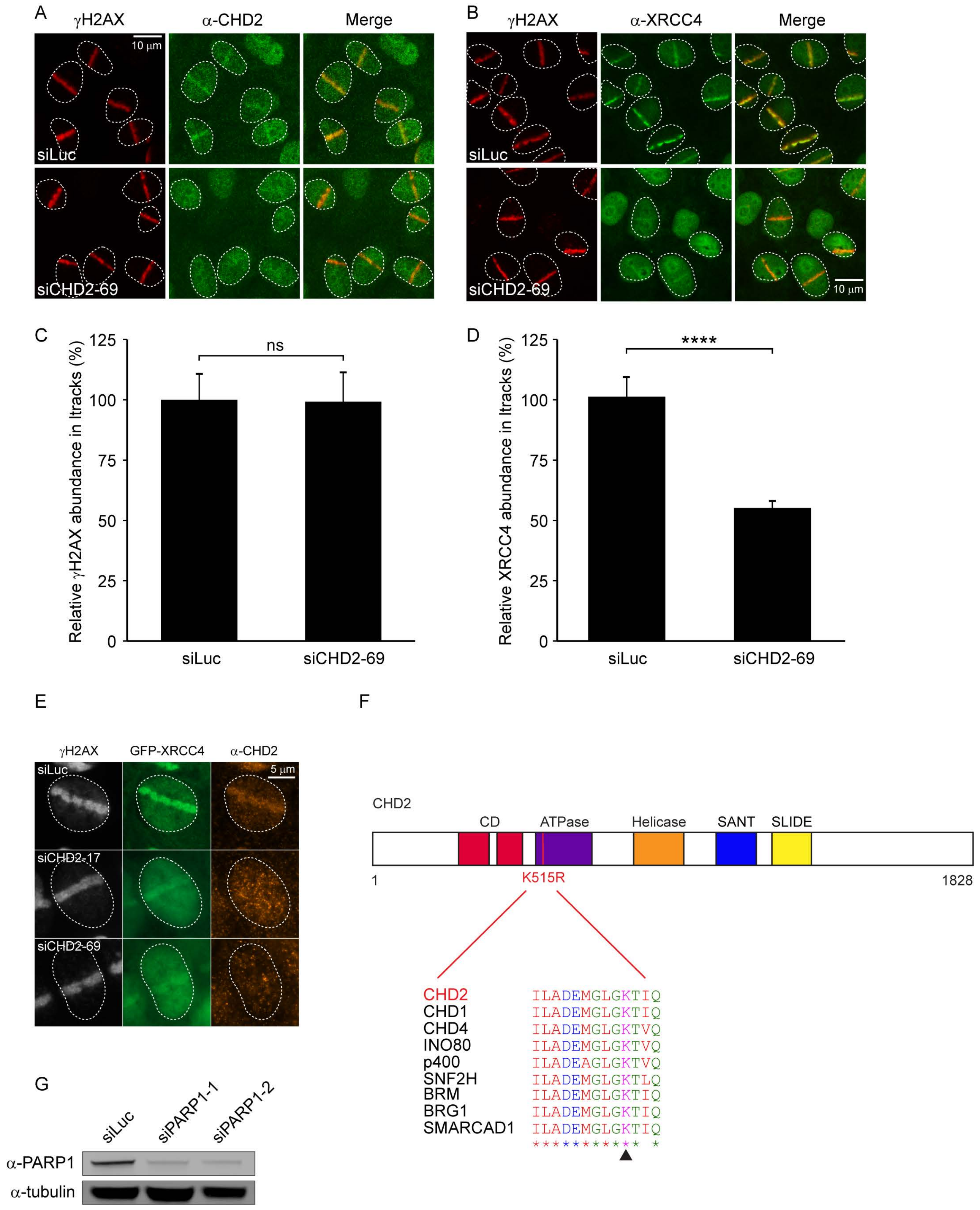
A
γH2AX
α-CHD2
Merge
10 µm
siLuc
siCHD2-69
B
γH2AX
α-XRCC4
Merge
siLuc
siCHD2-69
10 µm
C
Relative γH2AX abundance in Itracks (%)
125
100
75
50
25
0
ns
siLuc
siCHD2-69
D
Relative XRCC4 abundance in Itracks (%)
125
100
75
50
25
0
****
siLuc
siCHD2-69
E
γH2AX
GFP-XRCC4
α-CHD2
5 µm
siLuc
siCHD2-17
siCHD2-69
F
CHD2
CD
ATPase
Helicase
SANT
SLIDE
1
1828
K515R
CHD2 ILADEMGLGKTIQ
CHD1 ILADEMGLGKTIQ
CHD4 ILADEMGLGKTVQ
INO80 ILADEMGLGKTVQ
p400 ILADEAGLGKTVQ
SNF2H ILADEMGLGKTLQ
BRM ILADEMGLGKTIQ
BRG1 ILADEMGLGKTIQ
SMARCAD1 ILADEMGLGKTIQ
*********** *
G
siLuc
siPARP1-1
siPARP1-2
α-PARP1
α-tubulin

Figure S5. CHD2 promotes recruitment of XRCC4. Related to Figure 5. (A-B) U2OS cells were transfected with the indicated siRNAs, sensitized with BrdU and UV-A micro-irradiated. Cells were fixed and stained for (A) γH2AX and CHD2, or (B) γH2AX and XRCC4. (C-D) Quantification of the results from A and B. Between 60-90 cells were analysed from 2 independent experiments. Error bars represent the SEM. (E) U2OS cells expressing GFP-XRCC4 were transfected with the indicated siRNAs, micro-irradiated and stained for γH2AX and CHD2. (F) Schematic representation of the human CHD2 protein and its domains. A region corresponding to the conserved ATP-binding pocket is aligned to that of several other human chromatin remodellers. The arrow points to the conserved lysine at position 515 that was mutated to arginine (K515R) to serve as a dominant-negative in **Fig 5E**. (G) Western blot showing PARP1 knock-down efficiency for the indicated siRNAs in **Fig 5G** and **Fig 7E**. Statistical significance based on a two-tailed, unpaired t-test is indicated as: ****$p < 0.0001$, ***$p < 0.001$, **$p < 0.01$, *$p < 0.05$. ns, not significant.

Figure S6

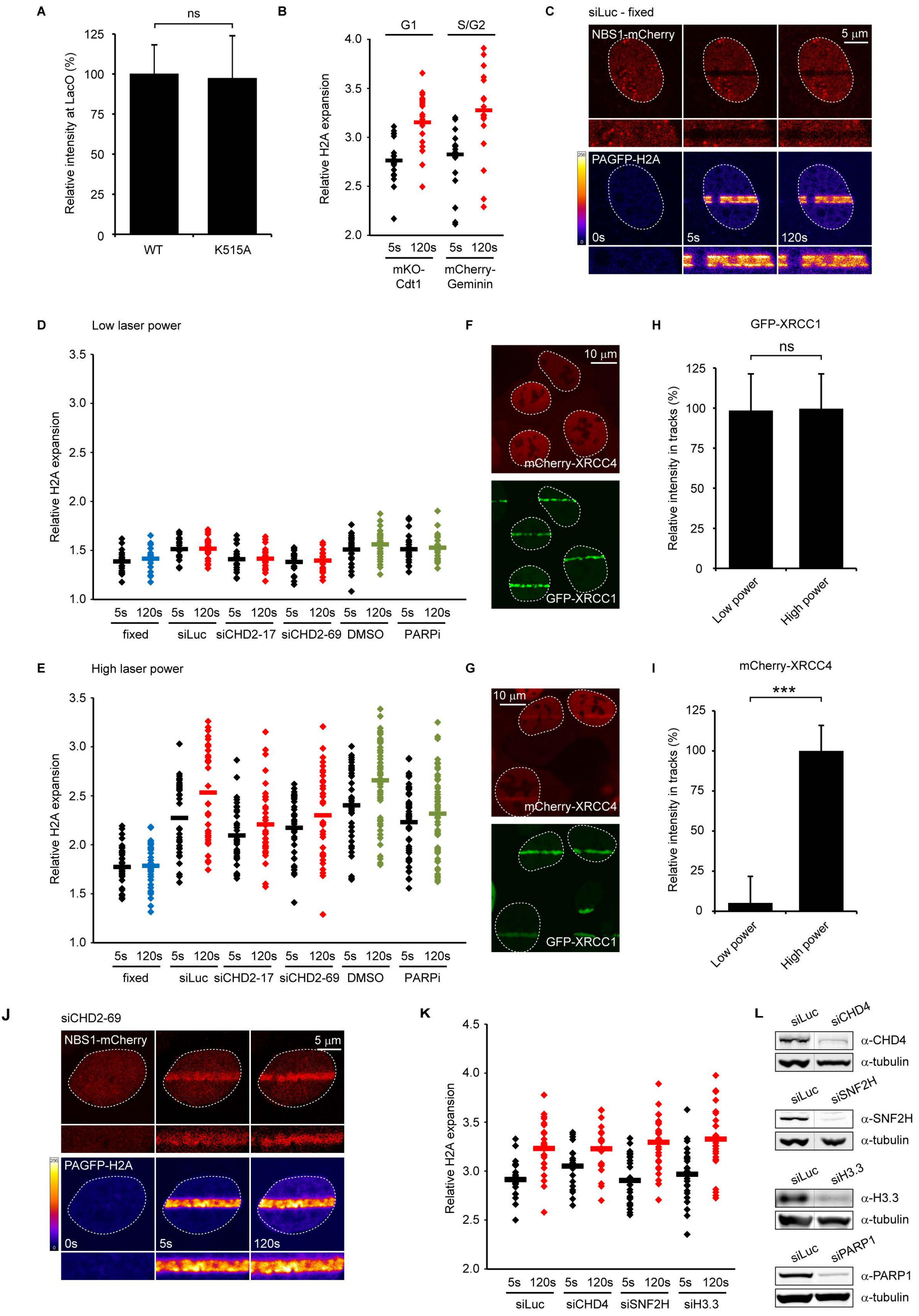
CHD2-GFP
A
ns
Relative intensity at LacO (%)
125
100
75
50
25
0
WT
K515A
B
G1
S/G2
Relative H2A expansion
4.0
3.5
3.0
2.5
2.0
5s
120s
5s
120s
mKO-Cdt1
mCherry-Geminin
C
siLuc - fixed
NBS1-mCherry
5 μm
PAGFP-H2A
256
0
0s
5s
120s
D
Low laser power
Relative H2A expansion
3.5
3.0
2.5
2.0
1.5
1.0
5s 120s 5s 120s 5s 120s 5s 120s 5s 120s 5s 120s
fixed
siLuc
siCHD2-17
siCHD2-69
DMSO
PARPi
E
High laser power
Relative H2A expansion
3.5
3.0
2.5
2.0
1.5
1.0
5s 120s 5s 120s 5s 120s 5s 120s 5s 120s 5s 120s
fixed
siLuc
siCHD2-17
siCHD2-69
DMSO
PARPi
F
10 μm
mCherry-XRCC4
GFP-XRCC1
G
10 μm
mCherry-XRCC4
GFP-XRCC1
H
GFP-XRCC1
ns
Relative intensity in tracks (%)
125
100
75
50
25
0
Low power
High power
I
mCherry-XRCC4
***
Relative intensity in tracks (%)
125
100
75
50
25
0
Low power
High power
J
siCHD2-69
NBS1-mCherry
5 μm
PAGFP-H2A
256
0
0s
5s
120s
K
Relative H2A expansion
4.5
4.0
3.5
3.0
2.5
2.0
5s 120s 5s 120s 5s 120s 5s 120s
siLuc
siCHD4
siSNF2H
siH3.3
L
siLuc
siCHD4
α-CHD4
α-tubulin
siLuc
siSNF2H
α-SNF2H
α-tubulin
siLuc
siH3.3
α-H3.3
α-tubulin
siLuc
siPARP1
α-PARP1
α-tubulin

Figure S6. DNA damage-induced chromatin changes correlate with the presence of DSBs. Related to Figure 6. (A) Quantification of the recruitment of CHD2$^{WT\text{-}GFP}$ or CHD2^{K515R}-GFP to the LacO array upon tethering αGFP-mCherry-LacR as shown in **Fig 6A**. 33-45 cells were analysed from 2 independent experiments. (B) Chromatin expansion in U2OS cells expressing PAGFP-H2A and either mKO-Cdt1 or mCherry-geminin. Cells were micro-irradiated to simultaneously induce DNA damage and photoactivate PAGFP. 20-22 cells were analysed from 2 independent experiments. (C) Absence of expansion of PAGFP-H2A tracks in fixed U2OS cells transfected with siLuc siRNAs. Note that NBS1-mCherry is bleached and does not accumulate. (D) U2OS cells expressing PAGFP-H2A were micro-irradiated to simultaneously induce DNA damage and photoactivate PAGFP. Low laser settings were used and no appreciable chromatin changes could be detected. (E) As in D, but with higher laser settings, which triggered substantial chromatin expansion. The average of this data is shown in **Fig 6F**. (F) Stable mCherry-XRCC4 cells were co-transfected with GFP-XRCC1 followed by micro-irradiation with low laser power as in D. mCherry-XRCC4 does not accumulate under these conditions, while robust GFP-XRCC1 recruitment is detected. (G) As in F, but following micro-irradiation with higher laser settings as in E. In addition to GFP-XRCC1, also mCherry-XRCC4 is recruited under these conditions, which also trigger pronounced DNA damage-induced chromatin changes as shown in E. The extent of (H) GFP-XRCC1 and (I) mCherry-XRCC4 recruitment under these conditions is quantified. 15-20 cells were analysed from 2 independent experiments. (J) Expansion of PAGFP-H2A tracks in U2OS cells transfected with the indicated siRNA in **Fig 6F**. NBS1-mCherry was as a DNA damage marker. (K) Quantification of chromatin expansion measured by PAGFP-H2A photo-activation in cells transfected with the indicated siRNAs. 22-27 cells were analysed from 2 independent experiments. Error bars represent SEM. (L) Western blot showing CHD4, SNF2H, H3.3 and PARP1 knockdown efficiency for the indicated siRNAs in K (CHD4, SNF2H, H3.3) and **Fig 6F** (PARP1). Statistical significance based on a two-tailed, unpaired t-test is indicated as: ****p < 0.0001, ***p < 0.001, **p < 0.01, *p < 0.05. ns, not significant.

Figure S7

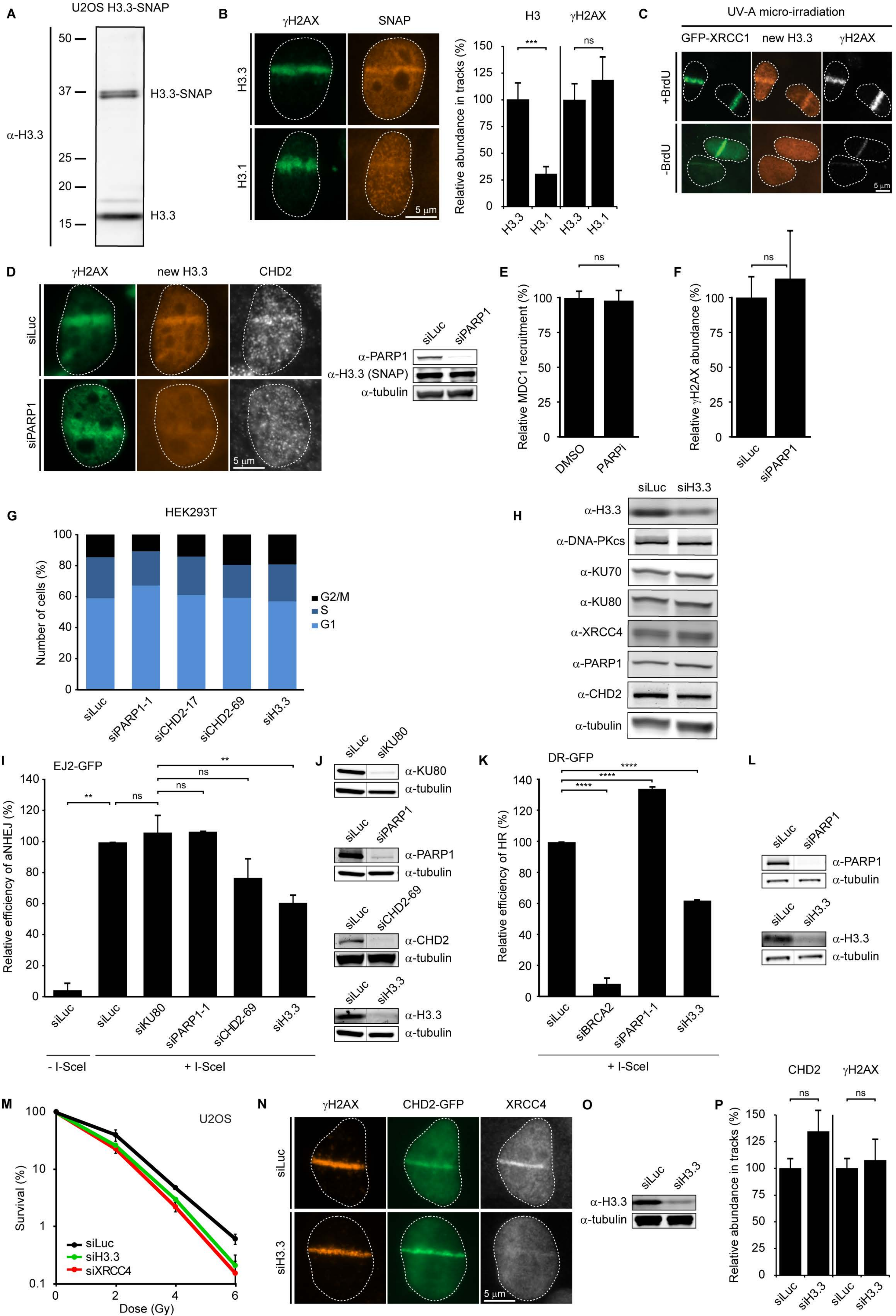
A
U2OS H3.3-SNAP
50
37
25
20
15
H3.3-SNAP
H3.3
α-H3.3
B
γH2AX
SNAP
H3.3
H3.1
5 µm
H3
γH2AX
***
ns
Relative abundance in tracks (%)
150
125
100
75
50
25
0
H3.3
H3.1
H3.3
H3.1
C
UV-A micro-irradiation
GFP-XRCC1
new H3.3
γH2AX
+BrdU
-BrdU
5 µm
D
γH2AX
new H3.3
CHD2
siLuc
siPARP1
5 µm
siLuc
siPARP1
α-PARP1
α-H3.3 (SNAP)
α-tubulin
E
ns
Relative MDC1 recruitment (%)
100
75
50
25
0
DMSO
PARPi
F
ns
Relative γH2AX abundance (%)
100
75
50
25
0
siLuc
siPARP1
G
HEK293T
Number of cells (%)
100
80
60
40
20
0
G2/M
S
G1
siLuc
siPARP1-1
siCHD2-17
siCHD2-69
siH3.3
H
siLuc
siH3.3
α-H3.3
α-DNA-PKcs
α-KU70
α-KU80
α-XRCC4
α-PARP1
α-CHD2
α-tubulin
I
EJ2-GFP
Relative efficiency of aNHEJ (%)
140
120
100
80
60
40
20
0
**
ns
ns
ns
**
siLuc
siLuc
siKU80
siPARP1-1
siCHD2-69
siH3.3
- I-SceI
+ I-SceI
J
siLuc
siKU80
α-KU80
α-tubulin
siLuc
siPARP1
α-PARP1
α-tubulin
siLuc
siCHD2-69
α-CHD2
α-tubulin
siLuc
siH3.3
α-H3.3
α-tubulin
K
DR-GFP
****
****
****
Relative efficiency of HR (%)
140
120
100
80
60
40
20
0
siLuc
siBRCA2
siPARP1-1
siH3.3
+ I-SceI
L
siLuc
siPARP1
α-PARP1
α-tubulin
siLuc
siH3.3
α-H3.3
α-tubulin
M
U2OS
Survival (%)
100
10
1
0.1
0
2
4
6
Dose (Gy)
siLuc
siH3.3
siXRCC4
N
γH2AX
CHD2-GFP
XRCC4
siLuc
siH3.3
5 µm
O
siLuc
siH3.3
α-H3.3
α-tubulin
P
CHD2
γH2AX
ns
ns
Relative abundance in tracks (%)
150
125
100
75
50
25
0
siLuc
siH3.3
siLuc
siH3.3

Figure S7. H3.3 acts at DSB sites to promote DNA repair. Related to Figure 7. (A) Western blot of U2OS cells stably expressing SNAP-tagged H3.3 showing expression of endogenous H3 and H3.3-SNAP. (B) Deposition of H3.3-SNAP compared to H3.1-SNAP at sites of DNA damage 5 min after UV-A micro-irradiation (left). For quantification (right) 23-26 cells were analysed from 2 independent experiments. (C) H3.3 deposition in untreated or BrdU-sensitized cells after UV-A micro-irradiation. GFP-XRCC1 and γH2AX were included as damage markers for single-strand breaks and DSBs, respectively. (D) H3.3-SNAP deposition in cells transfected with the indicated siRNAs. Cells were also stained for γH2AX and CHD2 (left). Western blot showing PARP1 knock-down efficiency (right). The quantification of this data is shown in **Fig 7H**. (E) Quantification of the recruitment of MDC1 in H3.3-SNAP cells treated with DMSO or PARPi from **Fig 7G**. (F) Quantification of the enrichment of γH2AX in H3.3-SNAP cells transfected with siLuc or siPARP1 from **Fig 7H**. (G) Cell cycle profile of HEK293T cells transfected with the indicated siRNAs. (H) Western blot showing that knock-down of H3.3 in U2OS cells does not affect the steady-state levels of CHD2, PARP1 or NHEJ proteins. (I) U2OS cells containing the EJ2-GFP reporter for aNHEJ were transfected with the indicated siRNAs and 48 hrs later co-transfected with an I-SceI expression plasmid and mCherry. The percentage of GFP/mCherry-positive cells was monitored by flow cytometry. The average of 2 experiments is shown. (J) Western blot showing KU80, PARP1, CHD2 and H3.3 knockdown efficiency for the indicated siRNAs in H. (K) As in H, but using HEK293T cells containing the DR-GFP reporter. (L) Western blot showing PARP1 and H3.3 knockdown efficiency for the indicated siRNAs in J. (M) Clonogenic survival after X-ray exposure in U2OS cells transfected with the indicated siRNAs. (N) U2OS cells expressing CHD2-GFP were transfected with the indicated siRNAs, UV-A micro-irradiated and stained for γH2AX and XRCC4. (O) Western blot showing H3.3 knockdown efficiency for the indicated siRNA in M. (P) Quantification of the results in N. 21-31 cells were analysed from 2 independent experiments. Error bars represent the SEM. Statistical significance based on a two-tailed, unpaired t-test is indicated as: $****p < 0.0001$, $***p < 0.001$, $**p < 0.01$, $*p < 0.05$. ns, not significant.

Table S1. List of CHD2-GFP-interacting proteins identified by mass spectrometry. Related to Figure 1. SILAC-labelled U2OS cells expressing GFP (L) or CHD2-GFP (H) were subjected to immunoprecipition using GFP Trap beads. Following trypsin digestion and desalting, eluted peptides of the H and L precipitates were mixed in a 1:1 ratio and analysed on a Q-Exactive Orbitrap mass spectrometer. Raw MS files were analysed with the MaxQuant software suite. The H/L ratios and number of unique peptides are indicated.

Extended Experimental Procedures

Cell lines. Human HEK293, VH10-SV40, RPE-1-hTERT, Phoenix and U2OS cells were cultured at 37°C in an atmosphere of 5% CO2 in DMEM, supplemented with antibiotics, 10% fetal calf serum and glutaMAX (Gibco). U2OS 2–6-3 cells containing 200 copies of a LacO-containing cassette (~4 Mbp) were a gift from Susan Janicki (Janicki et al., 2004). U2OS 2-6-3 cells stably expressing ER-mCherry-LacR-FokI-DD (Tang et al., 2013) were induced for 5 h by 1 µM Shield-1 (Clontech) and 1 µM 4-OHT (Sigma). HEK293T cells with stably integrated DR-GFP, EJ2-GFP or EJ5-GFP reporters were gifts from Jeremy Stark and Maria Jasin (Bennardo et al., 2008; Pierce et al., 1999). HeLa cells stably expressing KU70-GFP were a gift from Dik van Gent (Mari et al., 2006). U2OS cells stably expressing GFP-XRCC1 were a gift from Niels Mailand (Bekker-Jensen et al., 2007). U2OS cells stably expressing H3.1-SNAP were a gift from Sophie Polo (Adam et al., 2013). U2OS cells stably expressing GFP/mCherry-XRCC4, CHD2-GFP or H3.3-SNAP were generated by transfection and selection with puromycin (1 µg/ml) or G418 (400 µg/ml), respectively. U2OS cells stably expressing cell cycle markers mKO-Cdt1, mCherry-geminin or mAG-geminin were generated by lentiviral infection. VH10-hTERT cells stably expressing shRNAs (see list of shRNA sequences) were generated using retroviral infection. *Trf2*$^{-/-}$;*p53*$^{-/-}$;TRF2^{ts} MEFs harboring the temperature-sensitive TRF2^{I468A} (TRF2^{ts}) allele were generated from *Trf2*$^{flox/-}$ *p53*$^{-/-}$ MEFs as described previously (Konishi and de Lange, 2008; Peuscher and Jacobs, 2011). TRF2ts MEFs were maintained at the permissive temperature of 32 °C and only grown at 39 °C to induce telomere uncapping through inactivation of TRF2.

Chemicals. PARP inhibitor (KU-0058948) was a gift from Mark O'Connor (Astrazeneca) and used at a concentration of 1-10 µM.

Plasmids. The full-length human CHD2 cDNA (5.5 kb) was amplified by PCR from plasmid pCMV6-XL4-CHD2 (Open Biosystems) and inserted into pEGFP-N1 (Clontech). All indicated deletion mutants or point mutants of CHD2 were generated by PCR and cloning (see list of primers). siRNA-resistant CHD2 was generated by introducing the underlined mutations: GAAGGGAAGGGGCCCGGAAAG. The CHD2 Fragment 1392-1610 was inserted into GFP-NLS to ensure nuclear localization. The CHD2$^{1392\text{-}1610}$ and CHD2$^{1611\text{-}1828}$ cDNA fragments were inserted into pDEST15 in-frame with the GST-coding sequence. A collection of cDNAs encoding various chromatin remodelers was fused in-frame with either GFP in pEGFP-C1 (Clontech) (CHD4, CHD5, CHD6, CHD7, SNF2H, BRG1) or FLAG in pCDNA3.1 (Invitrogen) (CHD3, INO80). The H3F3B gene was fused in frame with GFP or a SNAP tag (New England Biolabs). pPAGFP-H2A was generated by replacing GFP with PAGFP in the previously described vector pGFP-H2A (Luijsterburg et al., 2012b). The VHH anti-GFP gene (Herce et al., 2013) (a gift of Heinrich Leonardt) was fused in-frame to mCherry-LacR. Lentiviral plamids encoding mKO-Cdt1, mCherry-geminin and mAG-geminin were kind gifts of Atsushi Miyawaki. The XRCC4 cDNA (a gift of Penny Jeggo) was inserted into EGFP-C3-ires-puro. GFP-C3-PARP1 was a gift of Valerie

Schreiber (Mortusewicz et al., 2007). The PARP1 cDNA was inserted into mCherry-LacR-C3. Vectors encoding mCherry-PARG^{wt} or mCherry-PARG^{E756D} were gift of Michael Hendzel (Ismail et al., 2012).

Transfections. Cells were transfected with plasmid DNA using Lipofectamine 2000 according to the manufacturer's instructions. Cells were typically imaged 24 hrs after transfection. All siRNA transfections (see list of siRNA sequences) were performed with 40 or 80 nM siRNA duplexes using Lipofectamine RNAiMAX (Invitrogen). Cells were transfected twice with siRNAs at 0 and 36 hrs and were typically analyzed 60 hrs after the first transfection.

Western blotting. Cell extracts were generated by cell lysis and boiled in sample buffer. Proteins were separated by sodium dodecyl sulfate polyacrylamide gel electrophoresis (SDS-PAGE) and transferred to nitrocellulose membranes. Protein expression was analyzed by immunoblotting with the indicated primary antibodies (see list of antibodies) and secondary CF680 Goat Anti-Rabbit IgG antibodies at 1:10.000, CF770 Goat Anti-Mouse IgG antibodies at 1:5000 and CF770 Goat Anti-Rat IgG antibodies at 1:10.000 (Biotium), and detection using the Odyssey infrared imaging scanning system (LI-COR biosciences, Lincoln, Nebraska USA) or ECL.

Generation of DSBs. IR was delivered by a YXlon X-ray generator (YXlon International, 200 KV, 4 mA, dose rate 1.1 Gy/min).

Cell survival assay. VH10-SV40 or U2OS cells were transfected for 48 h with siRNA. Alternatively, VH10-hTERT cells stably expressing shRNAs were used. Cells were trypsinized, seeded at low density and exposed to IR. After 7 days, the cells were washed with 0.9% NaCl and stained with methylene blue. Colonies of more than 20 cells were scored.

Immunoprecipitation for Co-IP. HEK293 cells were transfected with plasmids encoding GFP-PARP1 or CHD2-GFP. For endogenous IPs, the relevant antibody (or corresponding IgG control) was conjugated to Protein A-coupled agarose beads (Millipore 16-157). For immunoprecipitation, cells were lysed in EBC-150 buffer (50 mM Tris, pH 7.5, 150 mM NaCl, 0.5% NP-40, 1 mM EDTA) supplemented with protease and phosphatase inhibitor cocktails. The lysed cell suspension was sonicated 6 times for 10s on ice and subsequently incubated with 500 U Benzonase for 1 hr under rotation. The NaCl concentration was increased to 300 mM and the suspension was rotated for 20 min. The cleared lysates were subjected to GFP immunoprecipitation with GFP Trap beads (Chromotek) or PARP1/CHD2/KU70 immunoprecipitation with a specific antibody. The beads were then washed 4-6 times with EBC-300 buffer (50 mM Tris, pH 7.5, 300 mM NaCl, 0.5% NP-40, 1 mM EDTA) and boiled in sample buffer. For denaturing IPs, the beads were subsequently washed twice with EBC-1000 buffer (50 mM Tris, pH 7.5, 1 M NaCl, 0.5% NP-40, 1 mM EDTA). Bound proteins were resolved by SDS-PAGE and immunoblotted with the indicated antibodies.

Generation of mass spectrometry samples. For stable isotope labeling by amino acids in cell culture (SILAC) labeling, U2OS cells were cultured for 14 days in media containing ‘heavy’ (H) and ‘light’ (L) labeled forms of the amino acids arginine and lysine respectively. SILAC-labeled cells were transiently transfected with CHD2-GFP (H) or empty vector (L) and equal amounts of H- and L-labelled cells were lysed in EBC buffer as described above. CHD2-GFP (H) or empty vector control (L) lysates were subjected to immunoprecipition using GFP Trap beads as described above. The beads were subsequently washed 2 times with EBC-300 buffer and 2 times with 50 mM $(NH_4)_2CO_3$ followed by overnight digestion using 2.5 μg trypsin at 37°C under constant shaking. Peptides of the H and L precipitates were mixed in a 1:1 ratio and desalted using a Sep-Pak tC18 cartridge by washing with 0.1 % acetic acid. Finally, peptides were eluted with 0.1 % acetic acid/60 % acetonitrile and lyophilized.

Mass spectrometry. Mass spectrometry was performed essentially as previously described (Schimmel et al., 2014). Samples were analyzed on a Q-Exactive Orbitrap mass spectrometer (Thermo Scientific, Germany) coupled to an EASY-nanoLC 1000 system (Proxeon, Odense, Denmark). Digested peptides were separated using a 13 cm fused silica capillary (ID: 75 µm, OD: 375 µm, Polymicro Technologies, California, US) in-house packed with 1.8 µm C18 beads (Reprospher-DE, Pur, Dr. Maisch, Ammerburch-Entringen, Germany). Peptides were separated by liquid chromatography using a gradient from 2% to 95% acetonitrile with 0.1% formic acid at a flow rate of 200 nl/min for 2 hrs. The mass spectrometer was operated in positive-ion mode at 2.2 kV with the capillary heated to 200°C. Data-dependent acquisition mode was used to automatically switch between full scan MS and MS/MS scans, employing a top 10 method. Full scan MS spectra were obtained with a resolution of 70,000, a target value of $3x10^6$ and a scan range from 400 to 2,000 m/z. Higher-Collisional Dissociation (HCD) tandem mass spectra (MS/MS) were recorded with a resolution of 17,500, a target value of $1x10^5$ and a normalized collision energy of 25%. The precursor ion masses selected for MS/MS analysis were subsequently dynamically excluded from MS/MS analysis for 60 sec. Precursor ions with a charge state of 1 and greater than 6 were excluded from triggering MS/MS events. Raw MS files were analysed with the MaxQuant software suite (version 1.4.1.2; Max Planck Institute of Biochemistry).

Immunoprecipitation for PAR binding assays. HEK293 cells were transfected with plasmids encoding CHD2-GFP variants. For immunoprecipitation, cell were washed and collected by scraping in cold PBS and lysed on ice for 20 min in IP-300 buffer (50 mM Tris-HCl, 5 mM EDTA, 0.2 % NP-40, 300 mM NaCl, 0.5 mM PMSF) supplemented with protease inhibitors. Lysates were subsequently sonicated for 20 sec. An equal volume of IP-300 buffer without NaCl was added and the extracts were centrifuged at maximum speed at 4°C for 10 min. The supernatant was collected in a new tube and the chromatin pellet suspended in buffer containing 20 mM Tris-HCl pH 7.5, 100 mM KCl, 2 mM MgCl2, 1 mM CaCl2, 0.3 M sucrose, 0.1 % Triton X-100, protease inhibitor, phosphatase inhibitor and PMSF. The chromatin suspension was incubated with 800 U/ml MNase at room temperature for 30 min. MNase was stopped by addition of 5 mM EDTA and EGTA followed by microcentrifugation at maximum speed for 10 min at 4°C. The chromatin extract was combined with the collected supernatant and GFP immunoprecipitation was carried out for 12-15 hr at 4°C on a rotating stand using GFP trap beads (Chromotek). The beads were then washed five times with 50 volumes of Tris-buffered saline and 0.1 % tween (TBS-T) containing protease inhibitors and boiled for 10 min in Laemmli buffer.

Radioactive PAR synthesis. Radioactive PAR was synthesized as described earlier (Shah et al., 2011). Purified bovine PARP (6 U) was activated in 900 µl buffer containing 100 mM Tris-HCl pH 8.0, 10 mM $MgCl_2$, 10% glycerol, 10 mM DTT, 500 µM cold NAD, 250 µCi of 32P-NAD (adenylate-32P, 350 nM), 10 % ethanol and 23 µg activated calf thymus DNA. A 5 µl aliquot was retrieved to determine the initial counts per minute (cpm) in the mixture. The reaction was carried out at 30 °C for 30 min, followed by precipitation of auto-modified PARP1 on ice for 30 min, by adding 100 µl of 3 M Na-acetate pH 5.2 and 700 µl of isopropanol. The precipitated PARP1 was collected by spinning the tube at 13,000 rpm for 10 min at 4°C, washed two times with ethanol to remove the un-reacted NAD and air dried. The pellet was dissolved in 1 ml of 1 M KOH-50 mM EDTA, by heating at 60 °C for 1 hr to separate the PAR polymer from PARP1 and solubilize it. Subsequently, 9 ml of buffer AAGE9 (250 mM NH_4OAc, 6 M guanidine-HCl, 10 mM EDTA) was added and the pH was adjusted to 9. The mixture was loaded on 1 ml of DHBB resin in Econocolumns (BioRad), which was first equilibrated in 5 ml of water and 10 ml of AAGE9. The resin was washed with 20 ml of AAGE9 and 10 ml of NH_4-acetate (pH 9.0). The PAR polymer was eluted with 1 x 0.5 ml followed by 4 x 1 ml of water at 37 °C. Elutions were collected in separate Eppendorf tubes and counted on a β-counter. The concentration of PAR polymer was calculated based on the initial cpm (1 µl represents cpm/ 500 pmoles of NAD). Most radiolabelled PAR polymer was in the second elution, which was aliquoted and stored at -30 °C in a lead container.

Purification of GST-CHD2 fragments. GST-CHD2$^{1392-1610}$ and GST-CHD2$^{1611-1828}$ expression plasmids were transformed into BL21 cells, which were grown until the cells reached an OD600 of 0.6-0.8 absorbance units. To induce expression of the GST fusion proteins, 1 mM IPTG was added and cells were incubated for 4 hrs at 30 °C. After centrifugation, bacterial pellets were lysed at room temperature for 30 minutes in 2.5 ml lysis buffer (125 mM Tris, 150 mM NaCl, 1 mM $MgCl_2$ pH8, 0.1 volume BugBuster 10x, 2500 units rLysozyme, 62.5 units benzonase (Novagen-Merck), Protease Inhibitor Cocktail EDTA-free (Sigma-Aldrich)). Lysates were filtered through 0.2 µm filter membranes and incubated at room temperature for 1 hr with 500 µl Glutathione Superflow Agarose beads (Life Technologies). After binding, the Agarose beads were packed in a column and loaded on an ÅKTA chromatography system (GE Healthcare Biosciences). Columns were washed with Wash Buffer (WB; 125 mM Tris, 150 mM NaCl, pH8) and GST fusion proteins were eluted in WB containing 10 mM reduced glutathione (Sigma-Aldrich). Fractions with purified protein were collected and concentrated using Vivaspin ultrafiltration cups (Sartorius). Following concentration, the purified proteins were dissolved in 125 mM Tris, 150 mM NaCl, pH8, 10% glycerol. Purified proteins were frozen in liquid nitrogen and stored at -80 °C.

Southwestern blotting to monitor PAR and PARP1 binding. Immunoprecipitated CHD2-GFP proteins or recombinant GST-CHD2 proteins were separated in 8% SDS-PAGE denaturing gels. Purified human PARP1 was included as a positive control. Gels were incubated for 1 hr with gentle agitation in 20-30 ml of running buffer containing 5 % ß-mercaptoethanol. Proteins were then transferred to nitrocellulose membranes overnight at 35 V in a cold room. The membranes were rinsed three times in TST buffer (10 mM Tris 7.5, 150 mM NaCl, 0.05 % Tween) and incubated on a shaker at room temperature for 1 hr in the same buffer containing 250 nM radioactive PAR polymer. For CHD2-GFP studies, membranes were washed 3 times for 10 min with TST buffer, followed by 3 washes of 15 min each with the same buffer but containing 500 mM NaCl. The membranes were rinsed in the regular TST, dried and either exposed to a film or phosphoimager screen to detect radioactivity. Following the radioactive detection, membranes were blocked in PBS-MT (PBS with 5 % milk and 0.1 % tween), and probed for PARP1 followed by re-probing for GFP (see list of antibodies). For GST-CHD2 studies, membranes were washed 3 times for 10 min with TST buffer, followed by 3 washes of 10 min each with the same buffer but containing 500 mM NaCl. Membrane were rinsed with regular TST buffer, blocked in PBS-MT (PBS with 5 % milk and 0.1 % tween), and probed for PAR (10H) followed by re-probing for GST and PARP1 (see list of antibodies).

Immunofluorescent labelling. Cells were either directly fixed or pre-extracted with 0.25% Triton-X100 (Serva) in cytoskeletal (CSK) buffer (10 mM Hepes-KOH, 300 mM Sucrose, 100 mM NaCl, 3 mM $MgCl_{2,}$ pH 7.4) on ice for 2 min and subsequently fixed with 4% formaldehyde in PBS for 15 min at 4°C. Cells were post-extracted with 0.5% Triton-X100 (Serva) in PBS, and treated with 100 mM glycine in PBS for 10 min to block unreacted aldehyde groups. Cells were rinsed with phosphate-buffered saline and equilibrated in WB (PBS containing 0.5% BSA, and 0.05% Tween 20; Sigma-Aldrich). Antibody steps and washes were in WB. The primary antibodies (see list of antibodies) were incubated overnight at 4°C. Detection was done using goat anti-mouse or goat anti-rabbit Ig coupled to Alexa 488, 546 or 647 (1:1000; Invitrogen Molecular probes). Samples were incubated with 0.1 µg/ml DAPI and mounted in Polymount.

Microscopic analysis of fixed cells. Images of fixed samples were acquired on a Zeiss AxioImager M2 or D2 widefield fluorescence microscope equipped with 40x, 63x and 100x PLAN APO (1.4 NA) oil-immersion objectives (Zeiss) and an HXP 120 metal-halide lamp used for excitation. Fluorescent probes were detected using the following filters: DAPI (excitation filter: 350/50 nm, dichroic mirror: 400 nm, emission filter: 460/50 nm), GFP/Alexa 488 (excitation filter: 470/40 nm, dichroic mirror: 495 nm, emission filter: 525/50 nm), mCherry (excitation filter: 560/40 nm, dichroic mirror: 585 nm, emission filter: 630/75 nm), Alexa 555 (excitation filter: 545/25 nm, dichroic mirror: 565 nm, emission filter: 605/70 nm), Alexa 647 (excitation filter: 640/30 nm, dichroic mirror: 660 nm, emission filter: 690/50 nm). Images were recorded using ZEN 2012 software and analyzed in Image J.

Multiphoton laser micro-irradiation. U2OS cells grown on 18 mm coverslips were placed in a Chamlide CMB magnetic chamber and the growth medium was replaced by CO_2-independent

Leibovitz's L15 medium supplemented with 10% FCS and penicillin-streptomycin. Laser micro-irradiation was carried out on a Leica SP5 confocal microscope equipped with an environmental chamber set to 37°C. DSB-containing tracks (1.5 µm width) were generated with a Mira modelocked titanium-sapphire (Ti:Sapphire) laser (l = 800 nm, pulse length = 200 fs, repetition rate = 76 MHz, output power = 80 mW) using a UV-transmitting 63× 1.4 NA oil immersion objective (HCX PL APO; Leica). Confocal images were recorded before and after laser irradiation at 5 or 10 sec time intervals over a period of 2-3 min. PA–GFP-H2A was photo-activated using the same laser and settings as those used to inflict localized DNA damage.

UV-A laser micro-irradiation. U2OS cells were grown on 18 mm coverslips and sensitized with 10 µM 5′-bromo-2-deoxyuridine (BrdU) for 24 hrs as described (Acs et al., 2011; Luijsterburg et al., 2012a). For micro-irradiation, the cells were placed in a Chamlide TC-A live-cell imaging chamber that was mounted on the stage of a Leica DM IRBE widefield microscope stand (Leica) integrated with a pulsed nitrogen laser (Micropoint Ablation Laser System; Andor). The pulsed nitrogen laser (16 Hz, 364 nm) was directly coupled to the epifluorescence path of the microscope and focused through a Leica 40x HCX PLAN APO 1.25-0.75 oil-immersion objective. The growth medium was replaced by CO_2-independent Leibovitz's L15 medium supplemented with 10% FCS and penicillin-streptomycin and cells were kept at 37°C. The laser output power was set to 72 to generate strictly localized sub-nuclear DNA damage. Following micro-irradiation, cells were incubated for the indicated time-points at 37°C in Leibovitz's L15 and subsequently fixed with 4% formaldehyde before immunostaining. Typically, an average of 50 cells was micro-irradiated (2 iterations per pixel) within 10–15 min using Andor IQ software (Andor).

H3.3-SNAP labeling. U2OS cells stably expressing H3.3-SNAP were incubated with 10 µM SNAP-cell Block (New England Biolabs) in DMEM (10% FCS) for 30 min to quench pre-existing histones. Cells were incubated in fresh medium for 1.5 hrs to allow the synthesis of new H3.3 molecules and subsequently subjected to UV-A micro-irradiation. Following irradiation, newly synthesized H3.3-SNAP molecules were labeled with 2 µM SNAP-cell TMR star (New England Biolabs) in Leibovitz's L15 (10% FCS) for 15 min (pulse) after which cells were pre-extracted with 0.25% Triton-X100 (Serva, Heidelberg, Germany) in cytoskeletal (CSK) buffer (10 mM Hepes-KOH, 300 mM Sucrose, 100 mM NaCl, 3 mM MgCl2, pH 7.4) for 2 min and subsequently fixed with 4% formaldehyde.

Microscopic analysis of living cells. Images recorded after multi-photon micro-irradiation of living cells were analyzed using LAS-AF software (Leica). The average pixel intensity of laser tracks was measured within the locally irradiated area (I_{damage}), in the nucleoplasm outside the locally irradiated area ($I_{nucleoplasm}$) and in a region not containing cells in the same field of view ($I_{background}$). The relative level of accumulation expressed relative to the protein level in the nucleoplasm was calculated as follows: $((I_{damage} - I_{background})/(I_{nucleoplasm} - I_{background}) – 1)$. Track width was measured using ImageJ software.

Homologous Recombination (HR) and Non-Homologous End-Joining (NHEJ) reporter assays

HEK293 cell lines containing either a stably integrated copy of the DR-GFP, EJ5-GFP or EJ2-GFP reporter were used to measure the repair of I-*Sce*I-induced DSBs by HR or NHEJ (Bennardo et al., 2008; Pierce et al., 1999). Briefly, 48 h after siRNA transfection, cells were co-transfected with an mCherry expression vector and the I-SceI expression vector pCBASce (Pierce et al., 1999). 48 h later the percentage of GFP-positive cells among mCherry-positive cells was determined by FACS on a BD LSRII flow cytometer (BD Bioscience) using FACSDiva software version 5.0.3. Quantifications were performed using WinMDI 2.9 (freeware), FACSDiva™ (BD Biosciences) or FlowJo software (FlowJo).

Random plasmid integration assay

U2OS cells were seeded (day 1) and transfected with siRNAs in a 6 cm dish the following day (day 2). Later that day, the cells were transfected with 2 µg gel-purified BamHI-EcoRI-linearized pEGFP-C1 plasmid. The cells were subsequently transfected twice with siRNAs at 24 hrs and 36 hrs after the first transfection (day 3 and day 4, respectively). On day 5, cells were collected, counted and seeded in 15 cm dishes either lacking or containing 0.5 mg/mL G418. The transfection efficiency was determined on the same day by FACS analysis. The cells were incubated at 37°C to allow colony formation and medium was refreshed on day 8 and 12. On day 15, the cells were washed with 0.9% NaCl and stained with methylene blue. Colonies of more than 50 cells were scored. Random plasmid integration events on the G418-containing plates were normalized to the plating efficiency (plate without G418) and transfection efficiency based on GFP expression.

Chromosome fusions at uncapped telomeres assay

TRF2^{ts} MEFs were transduced with pLKO-puro shRNA lentiviruses obtained from Mission library clones (Sigma) containing shRNAs that target mouse *CHD2, PARP1, H3.3, LIGIV* or a scrambled control shRNA (see list of shRNA sequences). A retroviral shRNA and corresponding control shRNA was used for the knockdown of *LigaseIV* (Peuscher and Jacobs, 2011). Lentivirus and retrovirus production and transduction were performed as before (Peuscher and Jacobs, 2011). Following transduction, cells were selected on 4 µg/mL puromycin for 2-5 days. TRF2^{ts} MEFs infected with shRNAs constructs were shifted to the non-permissive temperature (39°C) for 24 hours to induce telomere uncapping. After 24 hrs of uncapping, cells were subjected to colcemide (Gibco) treatment for 2 hrs to enrich for metaphases. Cells were subsequently harvested by trypsinization, incubated for 7 min at 37°C in 75 µM KCl, and fixed in freshly prepared methanol:acidic acid (3:1). Cells were dropped onto wet slides and air-dried prior to hybridization (Boersma et al., 2015). Telomere-FISH was carried out by overnight hybridization with a TelC-FAM PNA probe. After hybridization, slides were washed and mounted in Vectashield containing DAPI (Vector Laboratories). Digital images of metaphases were captured using the Metafer4/MSearch automated metaphase finder system (MetaSystems) equipped with an AxioImager Z2 microscope (Zeiss). After scanning metaphase preparations at 10x magnification, high-resolution images of metaphases were acquired using a Plan-Apochromat 63x/1,40 oil objective.

siRNAs

Target	Sequence
BRCA2	GAAGAAUGCAGGUUUAAUAUU
CHD2-1	GAAACAACCUGCAUAUUUAUU
CHD2-17	GACAAGAACCAUCGCGAUUUU
CHD2-2	CAAGAACCAUCGCGAUUUAUU
CHD2-67	GGGUAAAUGUAGAGAGUGUUU
CHD2-68	GGGUUAAACUCCUGAAGUAUU
CHD2-69	GGGAAAAGGACCAGGGAAAUU
CHD2-70	AGAUUAACGUAGUGGUUUAUU
CHD4	GAGCGGCAGUUCUUUGUGAUU
DNA-PKcs	CUUUAUGGUGGCCAUGGAGUU
H3F3A	GAGAAATTGCTCAGGACTTUU
H3F3B	CAGAGGTTGGTGAGGGAGAUU
KU80	CAAGGAUGAGAUUGCUUUAGU
Luciferase (Luc)	CGUACGCGGAAUACUUCGAUU
PARG (Smart pool)	CCAGUUGGAUGGACACUAA GAUGGUAGUUCCUCCCAAA UACCAGAGCAGUUUAGUAA GGAAACGGUACUCUACUAA
PARP1-1	GAAAGUGUGUUCAACUAAUUU
PARP1-2	AAGAUAGAGCGUGAAGGCGAA
PARP2	AAGGAUUGCUUCAAGGUAAUU
SNF2H	GGAUUAAACUGGCUCAUUUUU
XRCC4	AUAUGUUGGUGAACUGAGAUU

shRNAs

Target	**Sequence**	**TRC number (Sigma Mission Library)**
ATM	GTAACATATGACCTCGAAA	
CHD2-a	GCAATATGGACTCTGAGAA	
CHD2-b	GTCTATGATATGCTT	
CHD2-c	GTAACATATGACCTCGAAA	
mouse CHD2-83	CGGATTCGCAGTTCCACTAAA	TRCN0000239016
mouse CHD2-85	TCATCCAGGCAGTACTATTAA	TRCN0000218567
mouse CHD2-87	CAAGAACCATCACGATTTAAT	TRCN0000239015
mouse H3F3A	GCGAGAAATTGCTCAGGACTT	TRCN0000012026
mouse H3F3B-1	GAGATCGCCCAGGATTTCAAA	TRCN0000311286
mouse H3F3B2	GAAGCTGCCATTCCAGAGATT	TRCN0000092921
mouse HIF	GCCCTAGATGGCTTTGTGA	
mouse LigIV	GGATCAGAGACGAGTTACT	
mouse PARP1-08	CCTCTTAGTCTGCTGAGCTTT	TRCN0000071208
mouse PARP1-48	TCGACGTCAACTACGAGAAAC	TRCN0000305948
mouse PARP1-59	GCCCTTGGAAACATGTATGAA	TRCN0000325059
mouse PARP1-959	GAGTACATTGTCTACGACATT	TRCN0000353959
mouse Scr	CAACAAGATGAAGAGCACCAA	

Antibodies

Antibody	Host	Company (reference)	IF	WB
CHD2	Rabbit	Cell signaling (4170)	1:100	1:1000
CHD2	Rat	Millipore (clone 8H3)		1:1000
CHD4	Mouse	Abcam (ab54603)		1:200
DNA-PKcs	Mouse	Abcam (ab1832)		1:500
FLAG	Mouse	Sigma (F 1804)	1:100	
GFP	Mouse	Roche (11814460001)		1:2000
GST	Rabbit	Cell Signaling (2625)		1:1000
H3.3	Rabbit	Millipore Cat.#09-838		1:1000
KU70	Mouse	Santa Cruz (sc-17789)		1:1000
KU80	Rabbit	Santa Cruz (sc-9034)		1:500
LigIV	Rabbit	Novus (#110-57379)		1:800
MDC1	Rabbit	Abcam (ab11171-50)	1:1000	
PAR (10H)	Mouse	Abcam (ab14459)	1:100	
PARP1	Rabbit	Cell Signaling (9542)		1:1000
PARP1	Rabbit	ENZO (ALX-210-302)		1:4000
PARP2	Mouse	ENZO (4G8)		1:200
SNF2H	Rabbit	Abcam (ab3749)		1:1000
tubulin	Mouse	Sigma (T6199)		1:5000
XRCC4	Rabbit	Gift from Dr. M. Modesti	1:500	
γH2AX	Mouse	Millipore (clone JBW301)	1:2000	

Primers

Name	**Sequence**
CHD2(1-461) FW	GGACTCGGTACCGCCACCATGATGAGAAATAAGGACAAAAG
CHD2(1-461) RV	GAGTCCACCGGTGGCAGGGCCTTGCATTCTCTTG
CHD2(462-951) FW	GGACTCGGTACCGCCACCATGAAGCAGAGACCACGATTTG
CHD2(462-951) RV	GAGTCCACCGGTGGCAGGATCGTCCGGCCAGTG
CHD2(952-1391) FW	GGACTCGGTACCGCCACCATGGAAAACAACTCAGGAAGGTC
CHD2(952-1391) RV	GAGTCCACCGGTGGTTTTTTTTTCATTGGACTTTTTTCCAAGC
CHD2(1392-1828) FW	GGACTCGGTACCGCCACCATGCAGAAGAAGAAAGAGAACAAG
CHD2(1392-1828) RV	GAGTCCACCGGTGGTGTTTTCCGAACATTCCAGTTATAATCTG
CHD2 (1610) RV	GAGTCCACCGGTGGGGCAGGCAAATGAGGCTTC
CHD2 (1611) FW	GGACTCGGTACCGCCACCATGTCCCATGGCCCACAGATGC
CHD2 K515R FW	GATGAAATGGGCCTAGGAGCGACCATCCAGACCATATC
CHD2 K515R RV	GATATGGTCTGGATGGTCGCTCCTAGGCCCATTTCATC

References

Acs, K., M.S. Luijsterburg, L. Ackermann, F.A. Salomons, T. Hoppe, and N.P. Dantuma. 2011. The AAA-ATPase VCP/p97 promotes 53BP1 recruitment by removing L3MBTL1 from DNA double-strand breaks. *Nat Struct Mol Biol*. 18:1345-1350.

Adam, S., S.E. Polo, and G. Almouzni. 2013. Transcription recovery after DNA damage requires chromatin priming by the H3.3 histone chaperone HIRA. *Cell*. 155:94-106.

Bekker-Jensen, S., K. Fugger, J.R. Danielsen, I. Gromova, M. Sehested, J. Celis, J. Bartek, J. Lukas, and N. Mailand. 2007. Human Xip1 (C2orf13) is a novel regulator of cellular responses to DNA strand breaks. *J Biol Chem*. 282:19638-19643.

Bennardo, N., A. Cheng, N. Huang, and J.M. Stark. 2008. Alternative-NHEJ is a mechanistically distinct pathway of mammalian chromosome break repair. *PLoS Genet*. 4:e1000110.

Boersma, V., N. Moatti, S. Segura-Bayona, M.H. Peuscher, J. van der Torre, B.A. Wevers, A. Orthwein, D. Durocher, and J.J. Jacobs. 2015. MAD2L2 controls DNA repair at telomeres and DNA breaks by inhibiting 5' end resection. *Nature*. 521:537-540.

Herce, H.D., W. Deng, J. Helma, H. Leonhardt, and M.C. Cardoso. 2013. Visualization and targeted disruption of protein interactions in living cells. *Nat Commun*. 4:2660.

Ismail, I.H., J.P. Gagne, M.C. Caron, D. McDonald, Z. Xu, J.Y. Masson, G.G. Poirier, and M.J. Hendzel. 2012. CBX4-mediated SUMO modification regulates BMI1 recruitment at sites of DNA damage. *Nucleic Acids Res*. 40:5497-5510.

Janicki, S.M., T. Tsukamoto, S.E. Salghetti, W.P. Tansey, R. Sachidanandam, K.V. Prasanth, T. Ried, Y. Shav-Tal, E. Bertrand, R.H. Singer, and D.L. Spector. 2004. From silencing to gene expression: real-time analysis in single cells. *Cell*. 116:683-698.

Konishi, A., and T. de Lange. 2008. Cell cycle control of telomere protection and NHEJ revealed by a ts mutation in the DNA-binding domain of TRF2. *Genes & development*. 22:1221-1230.

Luijsterburg, M.S., K. Acs, L. Ackermann, W.W. Wiegant, S. Bekker-Jensen, D.H. Larsen, K.K. Khanna, H. van Attikum, N. Mailand, and N.P. Dantuma. 2012a. A new non-catalytic role for ubiquitin ligase RNF8 in unfolding higher-order chromatin structure. *EMBO J*. 31:2511-2527.

Luijsterburg, M.S., M. Lindh, K. Acs, M.G. Vrouwe, A. Pines, H. van Attikum, L.H. Mullenders, and N.P. Dantuma. 2012b. DDB2 promotes chromatin decondensation at UV-induced DNA damage. *J Cell Biol*. 197:267-281.

Mari, P.O., B.I. Florea, S.P. Persengiev, N.S. Verkaik, H.T. Bruggenwirth, M. Modesti, G. Giglia-Mari, K. Bezstarosti, J.A. Demmers, T.M. Luider, A.B. Houtsmuller, and D.C. van Gent. 2006. Dynamic assembly of end-joining complexes requires interaction between Ku70/80 and XRCC4. *Proc Natl Acad Sci U S A*. 103:18597-18602.

Mortusewicz, O., J.C. Ame, V. Schreiber, and H. Leonhardt. 2007. Feedback-regulated poly(ADP-ribosyl)ation by PARP-1 is required for rapid response to DNA damage in living cells. *Nucleic Acids Res*.

Peuscher, M.H., and J.J. Jacobs. 2011. DNA-damage response and repair activities at uncapped telomeres depend on RNF8. *Nat Cell Biol*. 13:1139-1145.

Pierce, A.J., R.D. Johnson, L.H. Thompson, and M. Jasin. 1999. XRCC3 promotes homology-directed repair of DNA damage in mammalian cells. *Genes & development*. 13:2633-2638.

Schimmel, J., K. Eifler, J.O. Sigurethsson, S.A. Cuijpers, I.A. Hendriks, M. Verlaan-de Vries, C.D. Kelstrup, C. Francavilla, R.H. Medema, J.V. Olsen, and A.C. Vertegaal. 2014. Uncovering SUMOylation dynamics during cell-cycle progression reveals FoxM1 as a key mitotic SUMO target protein. *Mol Cell*. 53:1053-1066.

Shah, G.M., F. Kandan-Kulangara, A. Montoni, R.G. Shah, J. Brind'amour, M.D. Vodenicharov, and B. Affar el. 2011. Approaches to detect PARP-1 activation in vivo, in situ, and in vitro. *Methods Mol Biol*. 780:3-34.

Tang, J., N.W. Cho, G. Cui, E.M. Manion, N.M. Shanbhag, M.V. Botuyan, G. Mer, and R.A. Greenberg. 2013. Acetylation limits 53BP1 association with damaged chromatin to promote homologous recombination. *Nat Struct Mol Biol*. 20:317-325.